

Manuscript Details

Manuscript number	IJFATIGUE_2018_164_R1
Title	COMPUTED TOMOGRAPHY SCANNING OF THE INTERNAL MICROSTRUCTURE, CRACK MECHANISMS, AND STRUCTURAL BEHAVIOR OF FIBER-REINFORCED CONCRETE UNDER STATIC AND CYCLIC BENDING TESTS
Article type	Research Paper

Abstract

Fiber-reinforced concrete, its behavior, and the effects of cyclic loading on its internal microstructure are studied in this paper. A total of 65 prismatic specimens, in two different series, were tested: one designed with 1% and 2% of fibers by volume. Both fiber content and fiber orientation were measured using computed tomography (CT) scans. The results showed that the damage provoked a progressive reduction in the residual tensile strength. The differences in the behavior of both series were mainly related to their fiber content and, to a lesser extent, to their fiber orientation.

Keywords	fatigue; high strength concrete; fibre-reinforced concrete; residual tensile strength; CT-Scan technology
Taxonomy	Fiber-Reinforced Composite, Fatigue, Non-Destructive Testing, Fatigue Damage
Manuscript region of origin	Europe
Corresponding Author	Miguel Angel Vicente
Order of Authors	Miguel Angel Vicente, Jesús Minguéz, Dorys González Cabrera
Suggested reviewers	Thomas Schumacher, Heiko Herrmann, Riyadh Hindi

Submission Files Included in this PDF

File Name [File Type]

Cover Letter (2018-11).docx [Cover Letter]

Answer to reviewers (2018-11).docx [Response to Reviewers]

Paper Comparison (2018-11) (completo) (marked).docx [Revised Manuscript with Changes Marked]

Highlights.docx [Highlights]

Paper Comparison (2018-11) (completo).docx [Manuscript File]

Author Statement (2018-11).docx [Author Statement]

To view all the submission files, including those not included in the PDF, click on the manuscript title on your EVISE Homepage, then click 'Download zip file'.



UNIVERSITY OF BURGOS.
Department of Civil Engineering

Ph.D. Miguel A. Vicente.
Dpto. Ingeniería Civil. University of Burgos.
c/ Villadiego s/n. 09001. Burgos. Spain
E-Mail: mvicente@ubu.es

Burgos. Sunday, 25 November 2018

Dear Editor,

Please, find attached the review manuscript of the paper “COMPUTED TOMOGRAPHY SCANNING OF THE INTERNAL MICROSTRUCTURE, CRACK MECHANISMS, AND STRUCTURAL BEHAVIOR OF FIBER-REINFORCED CONCRETE UNDER STATIC AND CYCLIC BENDING TESTS”, co-authored by Jesús Mínguez, Dorys C. González, and myself.

This paper analyses the behaviour of Fiber Reinforced Concrete specimen subjected to cyclic 3-point bending test until failure and also until controlled damage. In addition, static post-cyclic load 3-point bending testing have been performed, to study the effect on the residual strength of the cyclic loads.

In addition, CT-Scan technology has been used to visualize the internal microstructure of the specimens, particularly the fibers, as the basis to correlate it with the macroscopic behavior.

All the information is new and it has not been published before nor is under consideration in any other Journal. We think it falls under the scope of your Journal and wish that it can be considered for publication in International Journal of Fatigue.

All the comments of the reviewers have been attended and, we've tried to include all of them in the new version of the paper. I also declare that there is no conflict of interest.

Sincerely,

Comments from the editors and reviewers:

-Reviewer 1

In the present paper the behavior of steel fiber concrete is investigated under cyclic, fatigue and quasi-static load conditions for two different fiber dosages. The fiber content and orientation in the crack region is analyzed using X-ray CT.

line 55: "X-rays are emitted in all directions" is misleading, the X-ray source is directional and the specimen under investigation is subjected to X-rays from all directions (in a plane) by rotation of either the specimen or the source and detector around the specimen.

ANSWER: I agree with you that the X-ray source is directional. I've tried to say that the X-rays are emitted and the detector measures and records the final X-ray intensity for all the X-rays. By rotating the specimen, a lot of different relative directions across the specimens are applied and, finally, every point of the sample is traversed by different X-rays, from different directions.

I've improved this paragraph in the new version of the paper.

line 92: average compressive strength given, but neither standard error or standard deviation. It would be good, if either of those would be presented as well.

ANSWER: The standard deviation of the concrete compression strength has been included.

line 136: "109" should probably be " 10^9 "

ANSWER: Done.

Table 2: I assume, the values presented are average. It would be good to present either standard error or standard deviation in addition.

ANSWER: Done.

Table 3: It would be good to present error estimates.

ANSWER: The error estimation can be defined in figure 9, where the Weibull fit is represented. In both cases, the Weibull curves show a good fitting, with R^2 values of 0.960 and 0.944 respectively.

This sentence has been included in the new version of the document.

Table 4: It would be good to present error estimates.

ANSWER: The error estimation has been included.

line 338/339: "Cracks ... tend to break." should probably be "Cracks ... tend to break the fiber."

ANSWER: You are right. This has been corrected.

Question: Although the efficiency factors (ie_x , ie_y , ie_z) are very common, in other fiber reinforced materials (e.g. plastics) other characteristics for the fiber orientation distribution are used, examples for these are the orientation tensor and scalar order parameter. To my knowledge, these also have been applied for fiber concrete. Did you try these?

ANSWER: We have only defined the fiber orientation using the efficiency factors, but not other orientation parameters. However, we'll take your comment into account for future works.

-Reviewer 2

The paper shows a very interesting study about the evolution of the internal damage originated in fiber-reinforced concrete subjected to cyclic flexural loadings. The article is very well organized and the work is novel, current and of great interest, so it is worthy to be published in IJF journal.

The weakest point of the research is the lack of information about the relationship between the internal structure of the material observed by CT and the mechanical behavior of the concrete. Authors have provided a very detailed information of the results obtained from CT scanning for different loading states, but they do not carry out an adequate analysis of how the microstructure influences the mechanical behaviors obtained. The fact of having two dosages of fibers modify the internal structure of the matrix and an analysis of how this phenomena affects the fatigue life of FRC with a comparison of similar investigations performed by other authors is missed.

ANSWER: The paper analyzes the effect of both fiber orientation and fiber content on the fatigue behaviour. First of all, there is not a significant difference between the fiber orientation in R-Series and in M-Series, so this parameter cannot be analyzed. Second, Table 3 shows that parameter β is the same in both cases, which denotes that fiber content has no influence on the S-N curve. This result agrees with the one obtained by Bankara and Ramanjaneyulu (2018), Goel and Singh (2014) and Johnson and Zemp (1991), among others.

In other words, two different concrete mixtures, with different fiber content, subjected, for example, to $S_{\max}=0.7$, show approximately the same fatigue life, although the maximum tensile stress is greater when the fiber content is greater.

Fibers alter the internal microstructure, by changing the porosity. However, this fact has no relevant influence on the fatigue life of the concrete specimens.

1 **COMPUTED TOMOGRAPHY SCANNING OF THE INTERNAL MICROSTRUCTURE, CRACK**
2 **MECHANISMS, AND STRUCTURAL BEHAVIOR OF FIBER-REINFORCED CONCRETE UNDER STATIC**
3 **AND CYCLIC BENDING TESTS**

4
5 Miguel A. Vicente^{1,2,*}, Jesús Mínguez¹, Dorys C. González^{1,2}.

6
7 ¹ Department of Civil Engineering, University of Burgos, c/ Villadiego, s/n, 09001, Burgos (Spain).

8 ² Department of Civil Engineering, Parks College of Engineering, Aviation and Technology, Saint Louis University, 3540
9 Lindell Blvd, Saint Louis, MO (USA).

10
11 * Corresponding Author: mvicente@ubu.es

12
13 Number of words: 5193

14 Number of tables and figures: 23

15
16 Keywords: fatigue, high strength concrete, fibre-reinforced concrete, residual tensile strength, CT-Scan technology.

17

19 **ABSTRACT**

20 Fiber-reinforced concrete (FRC), its behavior, and the effects of cyclic loading on its internal microstructure are studied
21 in this paper. Particular attention is given to the evolution of the residual tensile strength of the fiber-reinforced concretes and
22 damage following cyclic flexural loading. A numerical equation is also proposed to estimate the residual tensile strength,
23 depending on crack width, damage, fiber content, and fiber orientation. A total of 65 prismatic specimens, in two different
24 series, were tested: one designed with 1% of fibers by volume and the other with 2% of fibers. The specimens were not
25 notched, but had previously been subjected to pre-cracking, which has a similar effect to notching, although the specimens
26 become more vulnerable to fatigue. Both fiber content and fiber orientation were measured using computed tomography (CT)
27 scans. The results showed that the damage provoked a progressive reduction in the residual tensile strength. The differences
28 in the behavior of both series were mainly related to their fiber content and, to a lesser extent, to their fiber orientation.

29
30 **1. INTRODUCTION**

31 Fiber-Reinforced Concrete (FRC) is an increasingly widespread technical solution in civil engineering. It is a very
32 suggestive solution because of the reduction of the labor cost, especially if it is combined with self-compacting concrete. In
33 most cases, the addition of fibers improves the mechanical behavior of concrete: less cracking [1-3], improved fatigue life [4-
34 7], increased maximum tensile strength [8, 9], improved freeze-thaw behaviour [10, 11], and extended fatigue life [12, 13].

35 Fatigue in concrete may be understood as a process of mechanical weakening until failure. Cyclic loading causes the
36 emergence of microcracks and their enlargement inside the concrete mass, around internal defects, such as voids, etc. The
37 macroscopic consequences of fatigue are progressive changes in the mechanical parameters of the concrete.

38 Most research over recent years has focused on fatigue life, i.e., the number of loading cycles that the concrete element
39 can withstand, and the S-N curves, which correlate with the stress level and the fatigue life [14-25]. However, only very few
40 research works have focused on the mechanical parameters of concrete and their modification under cyclic loading [4, 6, 26-
41 35].

42 The weakening of FRC can be defined by changes in the residual tensile strength, $f_{R,i}$, following a number of cycles,
43 which is taken into account in the design of FRC structures. According to the Model Code 2010 [36], the structural design of
44 the FRC is based on the residual stress provided by the reinforcing fibres. In particular, the values of $f_{R,1}$ and $f_{R,3}$ are used in
45 the formulation, defined as the residual strength values associated with crack openings from 0.5 to 2.5 mm, respectively. In
46 the case of structural elements subjected to cyclic loading over time, a progressive decrease in the residual tensile strength is
47 expected [4, 6, 26], the minimum values of which are parameters to prevent unsafe designs.

48 Both the fatigue life and the loss of residual tensile strength strongly depend on the geometrical and mechanical
49 characteristics of the fibers (shape, length, slenderness, etc.), the number of fibers and fiber distribution and orientation within
50 the concrete matrix.

51 Regarding fiber distribution and orientation, Computed Tomography (CT) Scan technology is a powerful tool to study
52 the internal microstructure of the matter, and particularly, to study fiber distribution and orientation in the case of FRC. CT is
53 a non-destructive technique used to visualize the internal microstructure of materials based on the properties of X-rays. A CT-
54 Scan facility contains an intensity-controlled X-ray source and a detector, which measures the loss of X-ray intensity. **During**
55 **the scanning process, the X-rays are emitted and the detector measures and records the final X-ray intensity for all the X-rays.**
56 **By rotating the specimens, a lot of different relative directions across the specimen are applied and, finally, every point of the**
57 **sample is traversed by different X-rays, from different directions.**

58 During the post-scan data processing, the density at each point of the sample is obtained in accordance with the
59 measured loss of X-ray intensity for all the X-rays, since there is a relation between the loss of X-ray intensity and the density
60 of the matter that it passes through. The result is a 3D grey-scale image composed of voxels (ranging from 0 to 255), where
61 the grey value corresponds to the density of the voxel. Clear grey tones correspond to high densities while dark grey tones
62 correspond to low densities.

63 Beyond its traditional use in medicine, this technology is currently widely used in concrete research, especially in
64 fiber-reinforced concrete [37-43]. The enormous advantage of CT-Scan technology is that it permits the exact position, and
65 orientation of each individual fiber to be measured, which is otherwise impossible with other techniques. Moreover, the
66 combined use of CT-Scan technology with a macroscopic test is currently providing interesting results, since it is possible to
67 correlate the internal microstructure with the macroscopic response. A detailed explanation of CT-Scan technology and its
68 use in several engineering fields can be obtained in [44].

69 The aim of this research is to analyze how fiber content and fiber orientation influence fatigue life and residual tensile
70 strength in fiber-reinforced concrete specimens that have undergone static and cyclic three-point bending tests. Having ended
71 the cyclic loading test, the specimens were subjected to static testing until failure, and then their post-cracking residual
72 strengths were measured. The procedure developed by Gonzalez and co-workers [4, 6] was used.

73 The structure of this paper will be as follows: The experimental program will be presented in Section 2, the
74 experimental results will be described and discussed in Section 3, the failure mechanisms will be described in Section 4, and
75 finally, the conclusions will be presented in Section 5.

76

77 **2. EXPERIMENTAL PROGRAM**

78 In this section, the materials, the testing procedure and the scanning procedure will be described.

79 2.1 Materials

80 The whole test campaign had 65 prismatic specimens, belonging to two series: labelled R-Series and M-Series. In both
81 cases, the cement paste was the same and the only difference was the fiber content, which was 1% by volume in the R-Series
82 and 2% by volume in the M-Series (Table 1).

84 Table 1: Mix proportions

Materials	R-Series	M-Series
Cement (kg/m ³)	400	
Water (kg/m ³)	125	
Superplasticizer (kg/m ³)	14	
Silica fume (kg/m ³)	6	
Fine aggregate (kg/m ³)	800	
Coarse aggregate (kg/m ³)	1,080	
Fiber (% by volume)	1%	2%

85
86 Ordinary Portland cement, crushed limestone coarse and fine aggregates (maximum size 15 mm) were used. Hook-
87 end steel fibres of 50 mm in length and 1.0 mm in diameter were incorporated in the concrete, together with superplasticizer
88 Glenium 52 BASF and nanosilica MEYCO MS685 BASF additives. The concrete quality as per Eurocode 2 was C70/85 [45].
89 The specimens were cured for 180 days in a curing room at both a constant relative humidity of 100% and an ambient
90 temperature of 20°C. The specimens were then removed from the curing room and held under laboratory conditions until
91 testing. All the specimens were, at least, 300 days-old when the testing campaign began. So, the possible strength increase
92 during the fatigue test was minimized. The 28-day average compressive strength of the mixture was 81.5 MPa for the R-
93 Series and 78.1 MPa for the M-Series, with a standard deviation of 3.8 MPa and 4.3 MPa respectively.

94 A total of 40 R-Series prisms and 25 M-Series prisms were prepared. In all cases, the prism dimensions were 600 mm
95 in length, 150 mm in width and 150 mm in height. In addition, two sets of cylinders with a diameter of 150 mm and a height
96 of 300 mm were cast for further characterization of the concrete (mainly to obtain the compressive strength).

97

98 2.2 Testing procedure

99 The testing procedure for both series is well described in [4, 6]. In summary, the test program included the 4 phases
100 described as follows (Figure 1):

- 101 1. Phase 1: Initial crack. During the first phase, all the prismatic specimens were subjected to a three-point static
102 bending test until small cracks appeared. In this first phase, forty R-Series specimens and twenty-five M-Series
103 specimens were tested. The midspan cross-section of the specimens was not notched.
- 104 2. Phase 2: Fatigue tests. In the second phase, some specimens were subjected to a three-point cyclic bending test
105 to failure, in order to obtain the characteristic fatigue life of the material. In this second phase, twelve specimens
106 of the R-Series were tested, and nine specimens of the M-Series.
- 107 3. Phase 3: Cyclic tests. In the third phase, other specimens underwent a three-point cyclic bending test up to a
108 preset number of load cycles, with the aim of inducing controlled fatigue damage in the specimens. In this third
109 phase, twenty-one R-Series specimens and twelve M-Series specimens were tested
- 110 4. Phase 4: Static tests. In the last phase, all the specimens tested in the third phase plus the pre-cracked ones not
111 subjected to the cyclic tests underwent to a three-point static bending test. In this way, variations in the residual
112 tensile strength in relation to fatigue damage could be detected. In this fourth phase, twenty-eight specimens of
113 the R-Series were tested, and sixteen specimens of the M-Series.

114

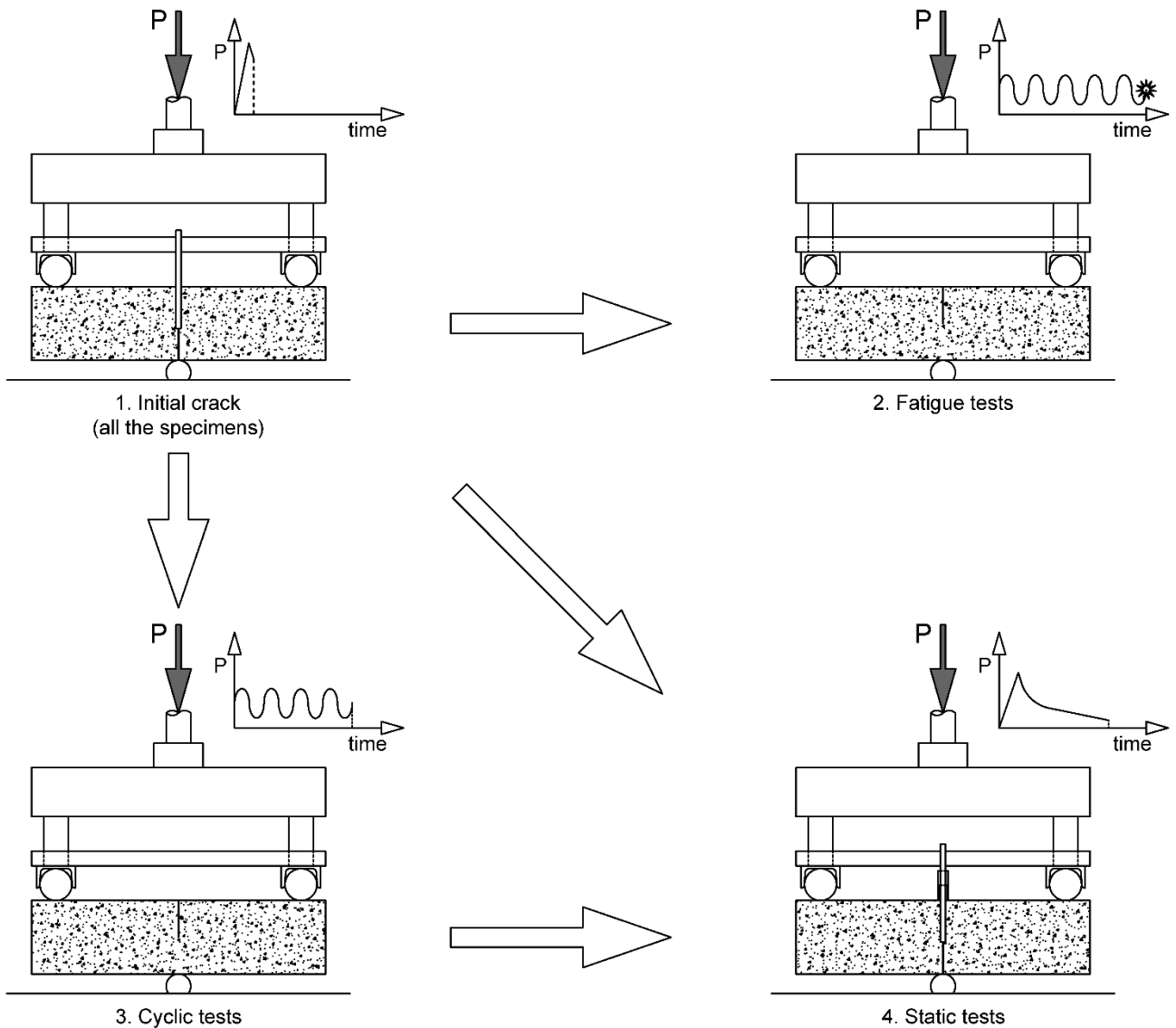


Figure 1: Explanation of the four test phases [4].

115

116

117 2.3 CT-Scan test

118 Additionally, computed tomography (CT) scans were performed to visualize the internal microstructure of concrete
 119 for further study. This technology permits a close examination of the fiber locations and orientations of each specimen. The
 120 fiber content has been directly taken from the mix dosage.

121 In this study, concrete specimens were CT-scanned by a GE Phoenix v|tome|x device equipped with a tube of 300
 122 kV/500W. The entire specimen was not scanned, but only a part of it, extracted from the central region, surrounding the crack
 123 (Figure 2). The scanning sample was 150 mm in height, 100 mm in width, and 50 mm in thickness.

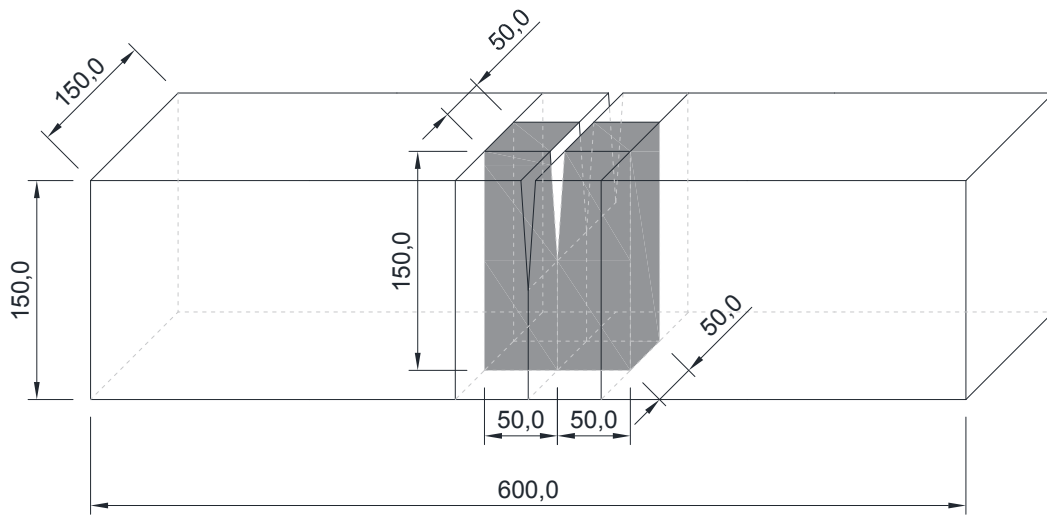


Figure 2: Location of the scanned piece from the whole prism.

124

125

126

127

This portion of the prism provides the most valuable information, since the fibers bridging the crack are the ones which control the cracking process.

128

129

Using a post-processing software, a total of 2,500 2D slices of 2048x2048 pixels (Figure 3) were obtained throughout the height of the specimen from the CT-scan machine. In this case, the horizontal resolution was $60 \times 60 \mu\text{m}^2$ and the vertical distance between the slices was $60 \mu\text{m}$ for a section with a diagonal length of 111.8 mm. After that a 3D image of the whole specimen was generated using all the above-mentioned 2D images. The post-processing software assigns a grey value to each voxel (volumetric pixel), coded as integer numbers between 0 and 255, where 0 equals black and 255 equals white. A value of 255 is assigned to the densest voxel and a value of 0 is assigned to the least dense voxel. For the rest of the voxels a linear relation is considered. The conclusion of the scanning process is a file including X, Y, and Z Cartesian coordinates of the voxel center of gravity and an integer number, from 0 to 255, regarding the density. The total number of voxels in a specimen was around $3.5 \cdot 10^9$.

137

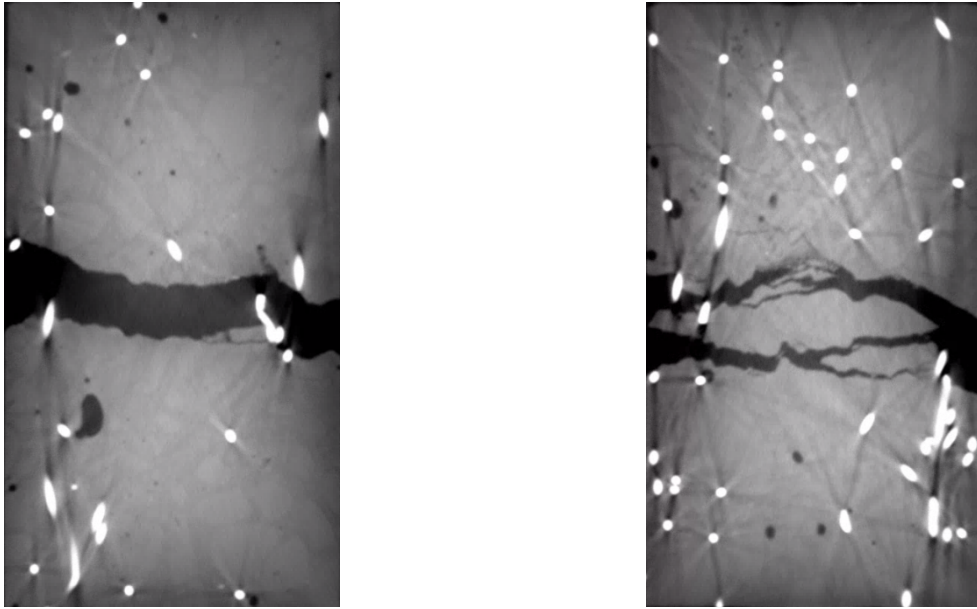


Figure 3: Slices belonging to different mixtures. From left to right: R-Series and M-Series.

The next step in this process is to identify and isolate each individual fiber inside the specimen with image analysis software. First of all, the software identifies the voxels belonging to voids, which show a range of grey values. In this case, once the histogram of grey scale is studied, the considered range for fibers was between 200 and 255 (Figure 4).

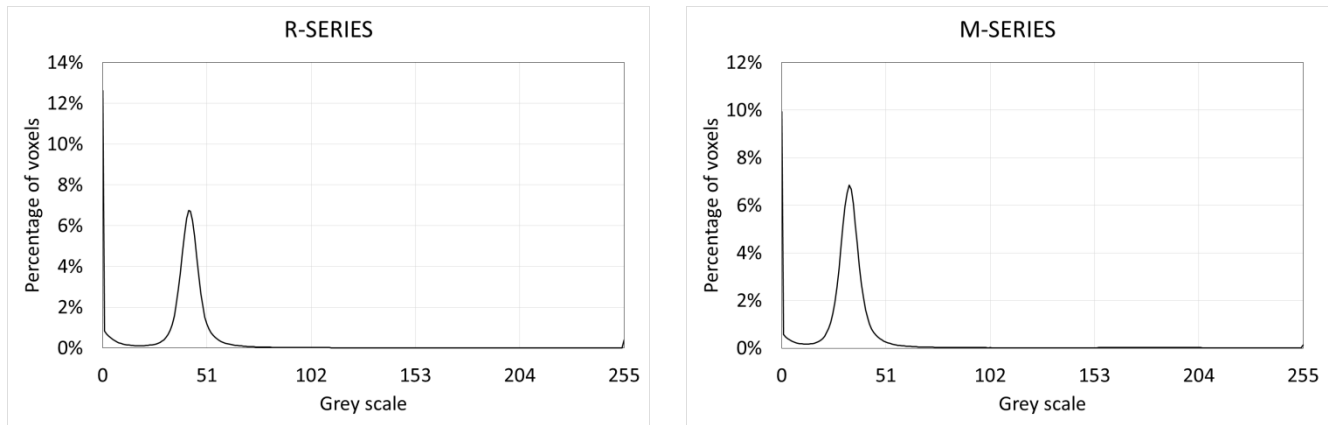
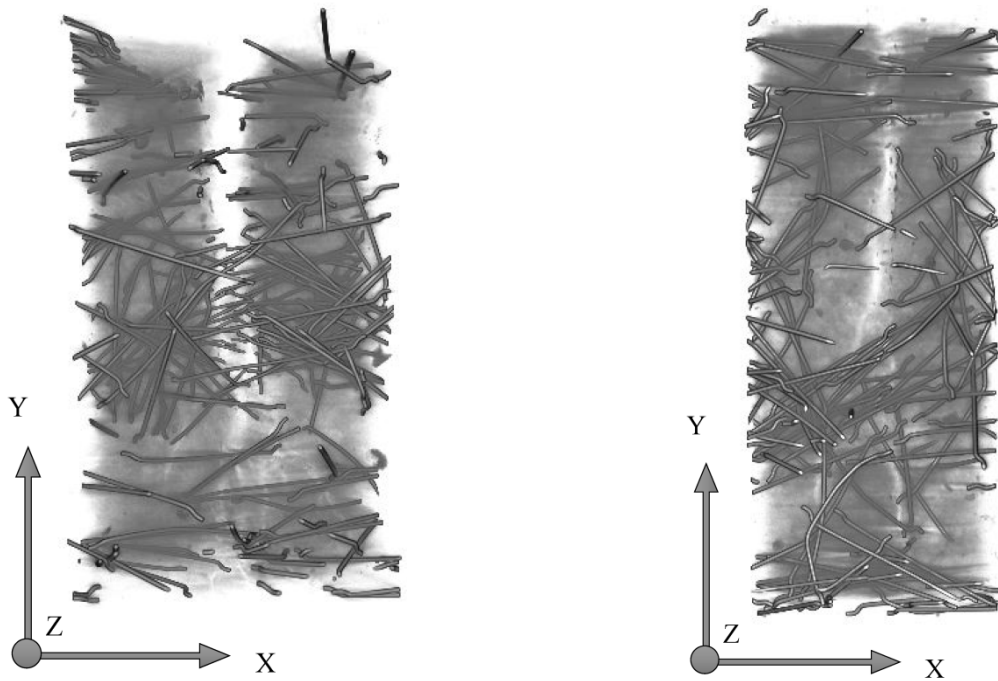


Figure 4: Histograms of grey scale.

Then, all the voxels in contact are merged, which come from the same fibers. The software identifies and isolates the different fibers. (Figure 5).



149

150

Figure 5: 3D views of the specimen belonging to different series. From left to right: R-Series and M-Series.

151

152

153

154

155

156

The final result of this image analysis is a dot matrix containing the Cartesian coordinates X , Y , and Z of the center of gravity of each fiber, the fiber length, and the orientation according to the Cartesian axis. In this case, the x -axis is transversal, the y -axis is longitudinal, and the z -axis is the vertical. The fiber orientation along the longitudinal axis is of interest, since it is related to the bridging of the crack. Figure 6 shows an isometric view of the fibers in a specimen from each series.

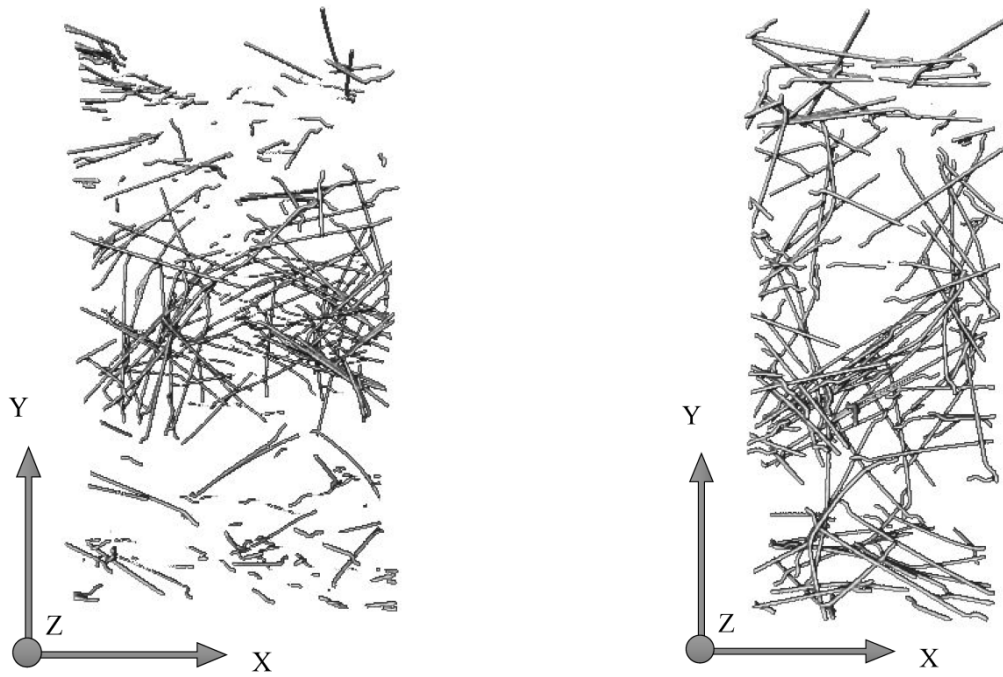


Figure 6: 3D views of the fibers belonging to different series. From left to right: R-Series and M-Series.

The CT-Scan device provides an enormous amount of useful information. However, it is not possible to obtain conclusions through direct observation of the 3D images alone. The data has to be post-processed using Digital Image Processing (DIP) software and/or post-processing sub-routines.

3. EXPERIMENTAL RESULTS

In this section, both the results of the CT-Scan and the results of the fatigue tests and the static post-cyclic tests will be presented. Finally, both the results from the CT-Scan and from the mechanical test will be correlated with each other.

3.1 CT-Scan analysis

Direct observation of the 3D images to distinguish the differences between both series is insufficient, and all the more so, for their quantification. In this case, the visualization and analysis software, AVIZO (FEI Visualization Sciences Group, Hillsboro, Oregon, USA), in combination with some sub-routines devised for the test were used to analyse the large data sets from the CT-Scan. The values shown in the different tables and figures refer to the average values of the specimens belonging to the same series.

174 3.1.1 Fiber content

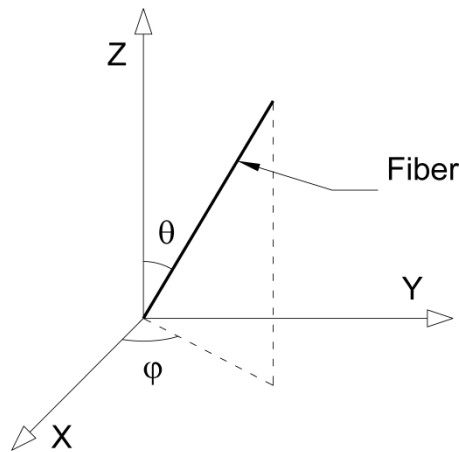
175 Using the CT-scan data on the full length of each individual fiber, the exact length of the fiber inside the scanned
176 sample can be computed. The total fiber volume may be obtained by multiplying this value by the section of the fiber. The
177 fiber content is defined as the quotient between the total fiber volume and the total volume of the sample.

178 In this case, the average fiber volumes were 0.98% for the R-Series and 1.97% for the M-Series. These values coincide
179 with the theoretical ones.

180

181 3.1.2 Fiber orientation

182 Fiber orientation is the most important result regarding the CT-Scan analysis. The primary angular information
183 provided by AVIZO are the values of both θ (theta) and ϕ (phi) (Figure 7). Theta is a polar angle, i.e., the angle between the
184 main axis of the fiber (the one containing its length) and the Z axis. Phi is the azimuthal angle, i.e., the angle between the
185 projection of the main axis on the XY plane and the X axis. Theta varies from 0° to 90° while phi varies from -90° to 90° .



186

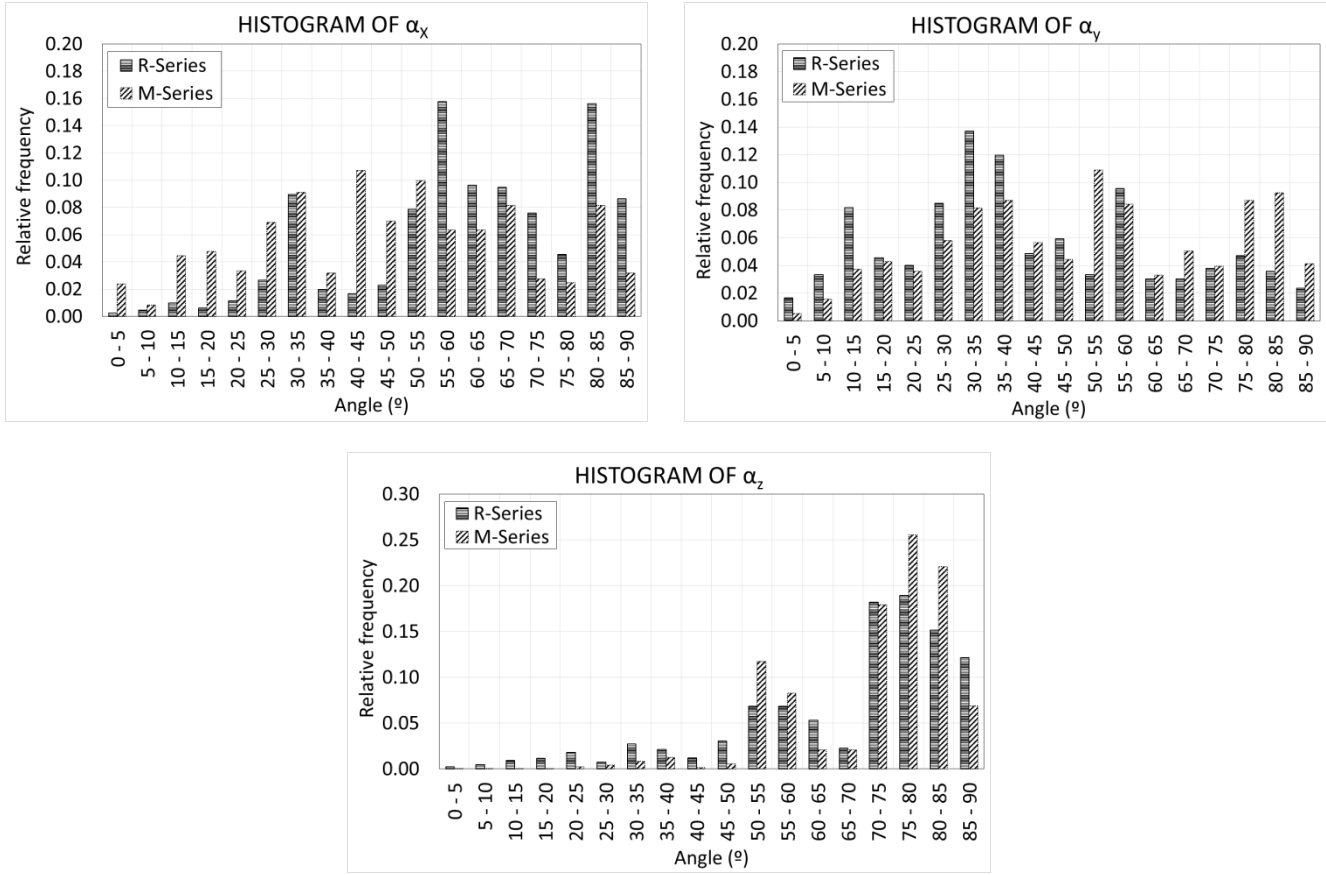
187 Figure 7: Identification of θ (theta) and ϕ (phi) angles

188 The angles according the Cartesian axis α_x , α_y and α_z can be obtained by the following expression (eq. 1):

$$\begin{aligned}\alpha_x &= \text{acos}[\sin(\theta) \cdot \cos(\varphi)] \\ \alpha_y &= \text{acos}[\sin(\theta) \cdot \sin(\varphi)] \\ \alpha_z &= \theta\end{aligned}\tag{1}$$

189 Next, the average histograms of angle distribution are shown, for both series (Figure 8).

190



191

192

193

194

195

196

197

198

199

200

Figure 8: Histograms of fiber orientation by Cartesian axis

In both cases, it is clearly observed that fibers are horizontally oriented, i.e., perpendicular to the z-axis, as the histogram of α_z shows that most of the fibers have an angle close to 90° . Regarding the x- and the y-axis of the M-Series, it appears that the fibers are randomly distributed along both axes. On the contrary, in the case of the R-Series, the fibers appear to show a slight tendency to remain parallel to the y-axis, since the histogram of α_x reveals that most of the fibers show an obtuse angle greater than 45° and the histogram of α_y reveals that most of the fibers show an acute angle under 45° .

The efficiency index (e_i) defines the numerical orientation along the x-, y- and z-axes by the following equation [43]

(eq. 2):

$$e_{i_x} = \sum_{i=1}^n f_{x,i} \cdot \cos(\bar{\alpha}_{x,i})$$

$$e_{i_y} = \sum_{i=1}^n f_{y,i} \cdot \cos(\bar{\alpha}_{y,i})$$

(2)

$$ei_z = \sum_{i=1}^n f_{z,i} \cdot \cos(\bar{\alpha}_{z,i})$$

201

202

where, $f_{x,i}$, $f_{y,i}$ and $f_{z,i}$ are the relative frequencies of each histogram bar, and $\bar{\alpha}_{x,i}$, $\bar{\alpha}_{y,i}$ and $\bar{\alpha}_{z,i}$ are the average values of the angles of each histogram bar. The efficiency index can show values from 0 to 1, where 0 means that all the fibers are oriented perpendicularly to the Z axis and 1 means that all the fibers are oriented parallel to the Z axis.

203

204

205

Table 2 shows the average values of the efficiency index of fibers for all series. In addition, the values in brackets represent the standard deviation.

206

207

208

Table 2: Efficiency index.

Series	ei_x	ei_y	ei_z
R-Series	0.44 [0.07]	0.70 [0.12]	0.35 [0.05]
M-Series	0.62 [0.11]	0.58 [0.10]	0.30 [0.05]

209

210

Observing the histograms in Figure 7, the R-Series shows a higher efficiency index along the y-axis, which means that the fibers tend to be oriented along the longitudinal axis. On the contrary, the M-Series shows that both ei_x and ei_y are quite similar, which means that the fibers are uniformly distributed along the XY plane. Regarding the z-axis, in both cases the value of ei_z is quite small, which means that the fibers tend to be oriented perpendicular to the z-axis, i.e., on the horizontal plane. Both series show a similar value of ei_z , so no relevant differences between them can be observed regarding this parameter.

211

212

213

214

215

216

As explained before, the most interesting efficiency index is ei_y , which represents the orientation of the fibers along the longitudinal axis, i.e., along the orthogonal direction to the crack surface.

217

218

219

3.1 Fatigue testings

220

Twelve prismatic specimens of the R-Series and nine prismatic specimens of the M-Series were tested under three-point cyclic bending tests up until fatigue failure. In all cases, no specimen had been pre-notched, but the specimens had been pre-cracked in a static three-point bending test until the first crack appeared. The previous damage significantly reduced the fatigue life [6].

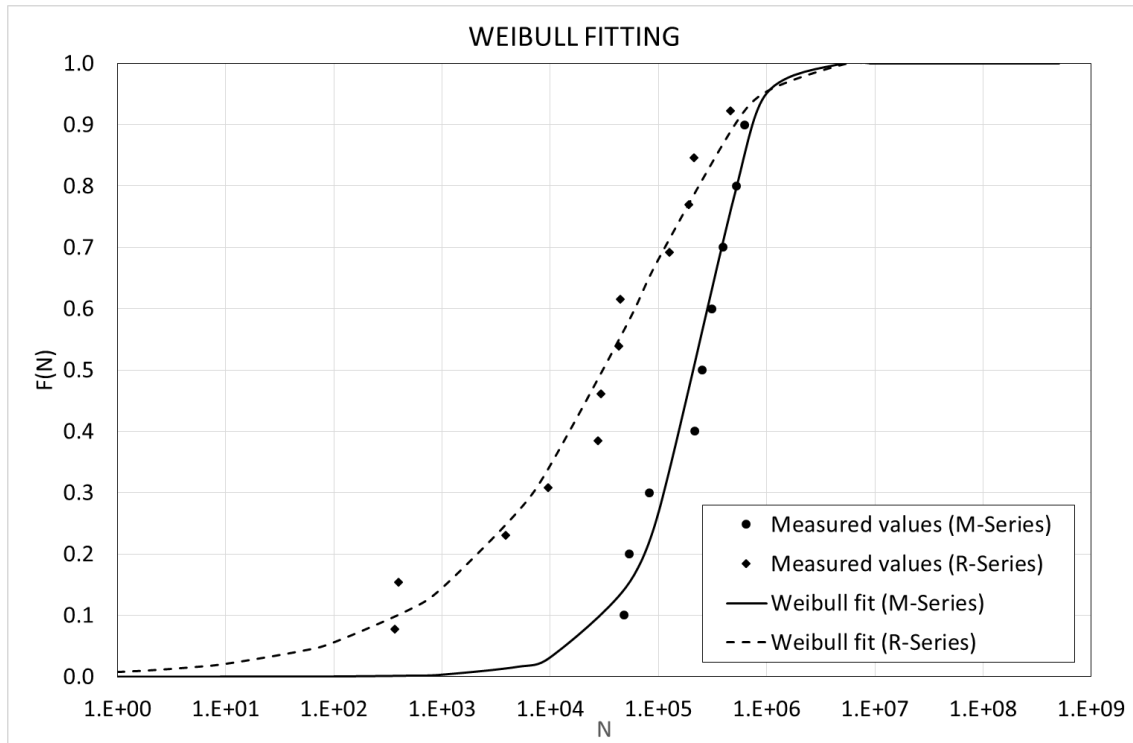
221

222

223

224 In the case of the R-Series, the cyclic load applied to each specimen ranged from 65% to 5% of its residual (or final)
 225 bending strength (obtained during the initial precracking test). In the case of the M-Series, the cyclic load ranged from 60%
 226 to 15% of its residual bending strength. The fatigue life of each series can be found in [4, 6].

227 By fitting the values to the Weibull distribution, the fatigue life of the different failure probabilities can be found for
 228 both series (Figure 9). In both cases, the representative fatigue life, N_{cr} , is defined as the number of cycles, N , corresponding
 229 to a failure probability of 20% ($P_f = 0.20$) (Table 5).



230
 231 Figure 9: Statistical distribution of fatigue life “N” and Weibull fitting for both series

232 In both cases the Weibull curves show a good fitting, with R^2 values of 0.960 and 0.944 respectively.

233 On the basis of these data, it is possible to define an S-N- P_f curve, in which the correlation between stress level, number
 234 of cycles, and failure probability is established. In this case, the Aas-Jakobsen’s S-N Expression is proposed [46-49] (eq. 3):

$$S = 1 - \beta \cdot (1 - R) \cdot \log_{10} N \quad (3)$$

235 where S is the relative stress level, R is the ratio between the maximum and the minimum stress values and β is a coefficient
 236 which represents the slope of the S-log(N) straight line [6]. Table 3 shows the values of β for both series.

237

238 Table 3: Representative fatigue life for both series and β coefficient.

	N_{cr}	β
R-Series	2260	0.113

M-Series	71094	0.110
----------	-------	-------

239

240

241

242

243

244

245

246

247

248

249

250

251

Table 5 shows that β is almost identical in both cases. This means that neither the fiber content nor the fiber orientation have influence on the parameter β . In consequence, β will only depend on the concrete matrix. This result agrees with the findings obtained by several research works [14, 26 and 27]. In these works, different concrete mixtures were performed considering different percentage of fibers, ranging from 0% (plain concrete) to 2%. The results of these research works also show almost identical S-N curves in all cases. Fibers alter the internal microstructure. However, this fact has no relevant influence on the fatigue life of the concrete specimen under tensile stress.

The above observation is not synonymous with the fiber content and/or the fiber orientation having no influence on the fatigue life. It is noteworthy that S is the relative stress value, i.e. the quotient between the maximum stress value σ_{max} and the flexural tensile strength of the concrete $f_{ct,fl,pre}$, obtained from the precracking test. The fiber content and orientation influence the value of $f_{ct,fl,pre}$. The higher the fiber content, the higher the value of $f_{ct,fl,pre}$, and the higher the efficiency index, the higher the value of $f_{ct,fl,pre}$. However, when the same relative maximum tensile strength S_{max} is applied to different concrete mixtures, showing different fiber content and/or fiber orientation, the fatigue life is the same.

252

3.2 Static testings of the specimens previously subjected to cyclic load

253

254

255

As explained before, some of the prisms were subjected to cyclic loads up to predefined level of damage. According to the Palmgren-Miner criterion, damage is defined as the quotient between the number of cycles and the fatigue life. In this case, fatigue life has been defined as the number of cycles showing a failure probability of 0.2 (Table 5).

256

257

258

For the R-Series, four groups of 7 prisms each were tested until reaching damage levels of 0.00, 0.20, 0.80 and 0.90, respectively. During the cyclic test, one specimen in the third group and one specimen in the fourth group collapsed before reaching the preset number of cycles.

259

260

261

Moreover, four groups of 4 prisms each were tested for the M-Series, up until damage levels of 0.00, 0.03, 0.28, and 2.81, respectively. In this case, during the cyclic test, one specimen belonging the fourth group collapsed, before reaching the preset number of cycles.

262

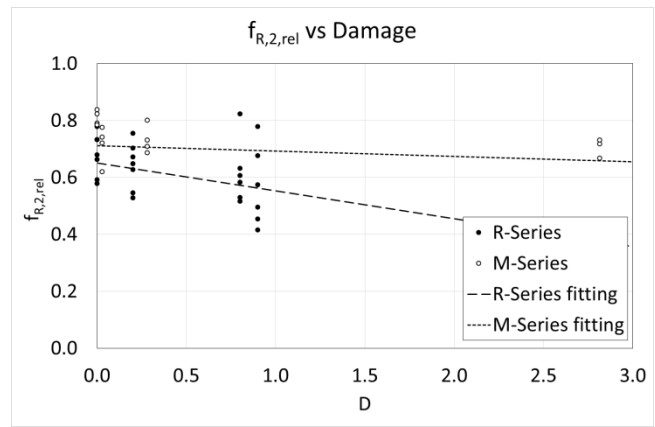
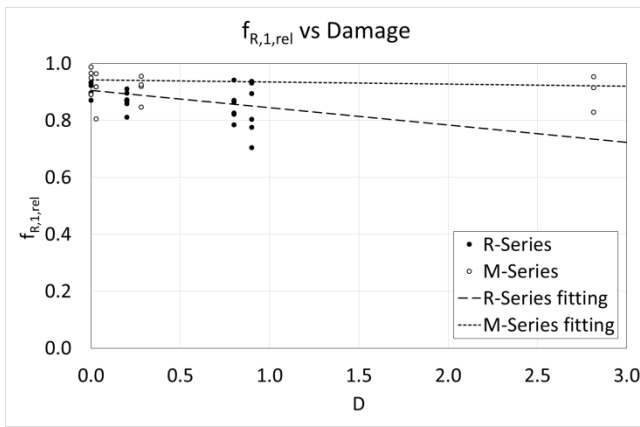
263

264

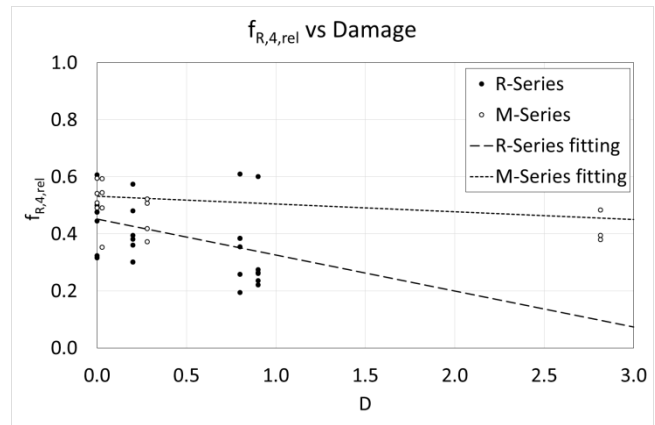
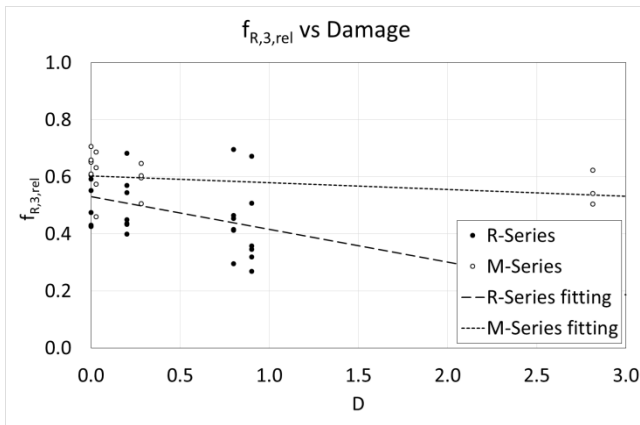
Figure 10 shows the values of the relative residual tensile strength ($f_{R,i,rel}$) for the both series and for the different values of damage [4, 6]. In addition, trend lines are drawn, for easy visualization of the variation in the relative residual tensile strength of the damage.

265

266



267



268

Figure 10: Variation of the relative residual tensile strength to the damage, for both series.

269

270

271

272

273

274

As can be observed in Figure 10, in all the cases, the relative residual tensile strength decreased with the damage. This decrease can be observed in both the R-Series and the M-Series. In the case of the R-Series, the trend lines are always placed below those of the M-Series. Furthermore, these lines show a decreasing slope greater than those of the M-Series. This is directly related to the fiber content. It is clearly observed that the higher the fiber content, the higher the relative residual tensile strength.

275

276

277

Figure 11 shows these same data in a different way, i.e. it shows the correlation between the relative residual tensile strength with the crack width (w), for the different damage and for the different series [4, 6]. Additionally, trend lines have been drawn, in order to easily visualize the variation of the relative residual tensile strength to the crack width.

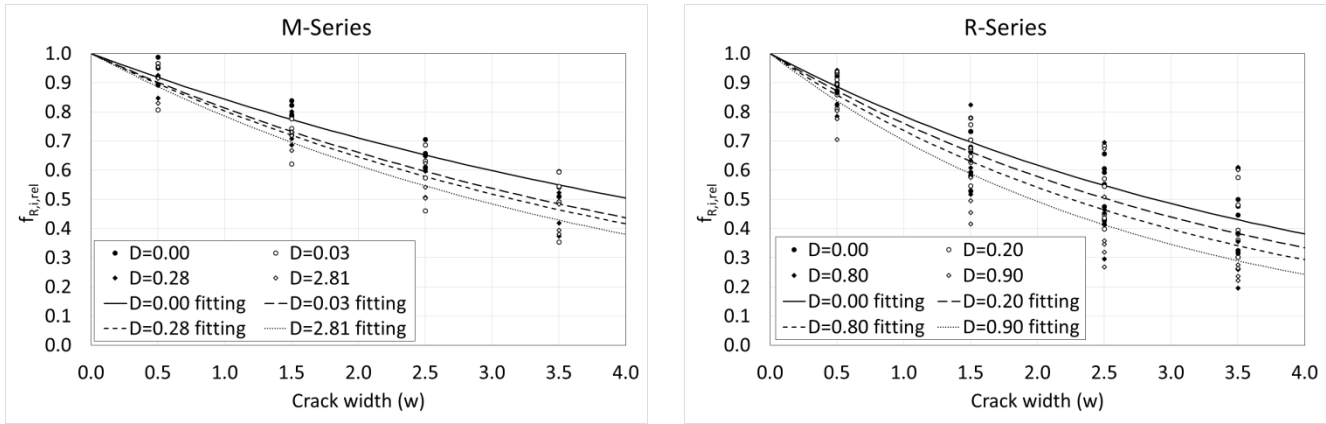


Figure 11: Variation of the relative residual tensile strength to the crack width, for both series.

Again, it can be observed that the trend lines show a progressive decrease with the damage, i.e., the higher the damage, the higher the negative slope of the line is. This behavior is observed in both series.

It can again be seen that the trend lines show a progressive decrease with the damage, i.e., the higher the damage, the higher the negative slope of the line; a behavior observed in both series.

When both series were compared, it was noted that the trend lines of the M-Series showed a smaller slope than those of the R-Series, which demonstrate again that the relative residual tensile strength is inversely proportional to the fiber content.

In the work carried out by Gonzalez and co-workers in 2018 [4], an exponential fitting is proposed for the average values of relative residual tensile strength, which is as follows (eq. 4).

$$f_{R,i,rel} = \exp\{-a_D \cdot w\} \quad i:=1 \text{ to } 4 \quad (4)$$

where, $f_{R,i,rel}$ is the relative residual tensile strength, ($i:=1$ to 4) and w is the crack width. The fitting coefficient, a_D , depends on the damage. Table 4 shows the values of a_D for the different damage values in both series. Additionally, Figure 12 shows these values in a graphic way with their fitted curves.

Table 4: Values of a_i for both series, depending on the damage levels.

R-Series			M-Series		
D	a_i	R^2	D	a_i	R^2
0.00	0.241	0.940	0.00	0.171	0.990
0.20	0.274	0.945	0.03	0.207	0.994
0.80	0.307	0.954	0.28	0.219	0.971
0.90	0.354	0.965	2.81	0.242	0.997

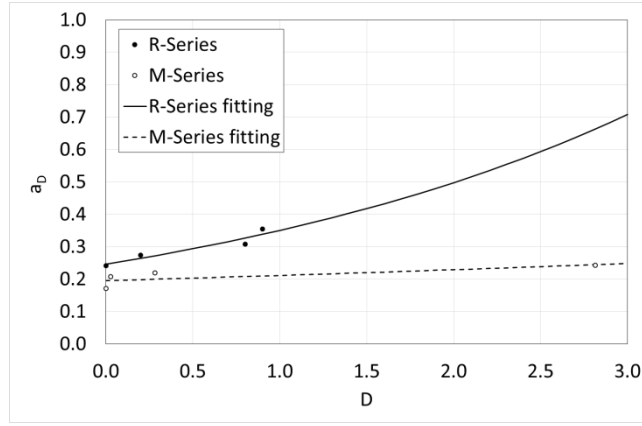


Figure 12: Values of a_D for both series, depending on the damage levels

295

296

297

298

299

300

301

302

303

304

305

306

307

308

309

In Table 6 and Figure 12, the M-Series show smaller values of a_D for all damage levels. Furthermore, the increase of a_D is greater in the case of the R-Series than in the case of M-Series, which once again shows that a_D depends on the fiber content, in such a way that the higher the fiber content, the smaller the slope of the curve a_D vs D . Moreover, the fiber orientation influences the behavior, especially of the crack-bridging fibers.

Two extreme cases may be studied, in order to develop a proper physically compatible equation for a_D .

The first extreme case is, on the one hand, when the fiber content is zero, that is, plain concrete. In this case, $a_i = \infty$ because, plain concrete shows null values of relative residual tensile strength.

On the other hand, when the fiber content increases, a_D decreases, which also implies loss of relative residual tensile strength (see eq. 4). In an extreme case, when the fiber content is 100%, the hypothesis of $a_i = 0$ is considered.

Regarding fiber orientation, when the efficiency index is zero, fibers are placed parallel to the crack surface, $a_i = \infty$, and the behavior is not dissimilar to plain concrete. In addition, when the efficiency index increases, a_D decreases.

According to these criteria, the following fitting formula is proposed (eq. 5):

$$a_i = \frac{\alpha}{e^{i_y}} \cdot \left(\frac{100 - f}{f} \right)^{0.7} \exp \left\{ \beta \cdot \left(\frac{100 - f}{f} \right)^{2.1} \cdot D \right\} \quad (5)$$

310

where, f is the fiber content (in percent), and α and β are two fitting coefficients. This equation is compatible with the above-mentioned criteria. In this case, the best fitting is obtained for $\alpha = 6.90 \cdot 10^{-3}$ and $\beta = 2.27 \cdot 10^{-5}$.

312

313

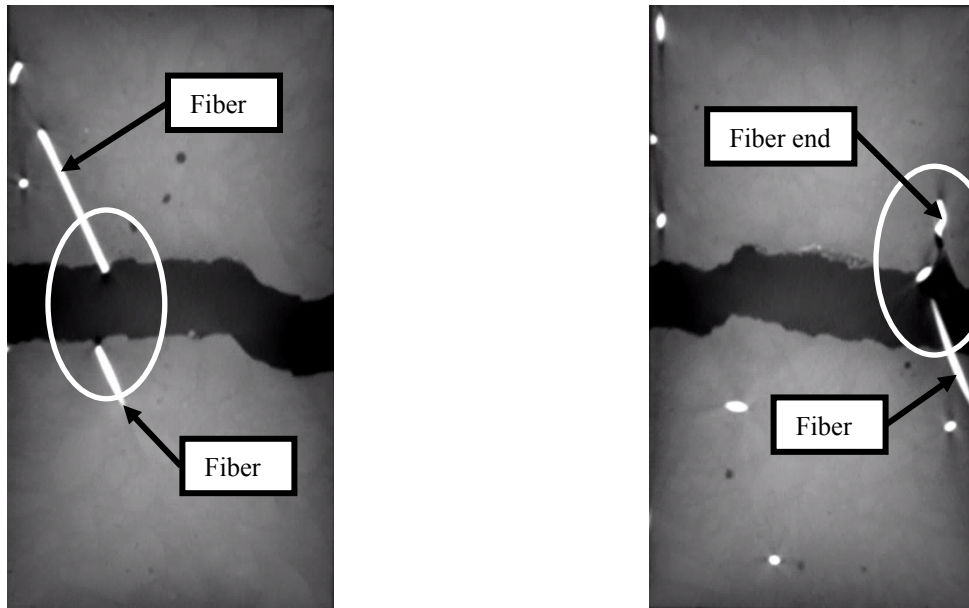
4. FAILURE MECHANISMS

314

Using the CT-Scan, it is possible to visualize the failure mechanisms that occur inside the prism, in areas surrounding the crack. In general, two mechanisms can be observed: fiber breakage and failure of the fiber anchorage. The first one depends

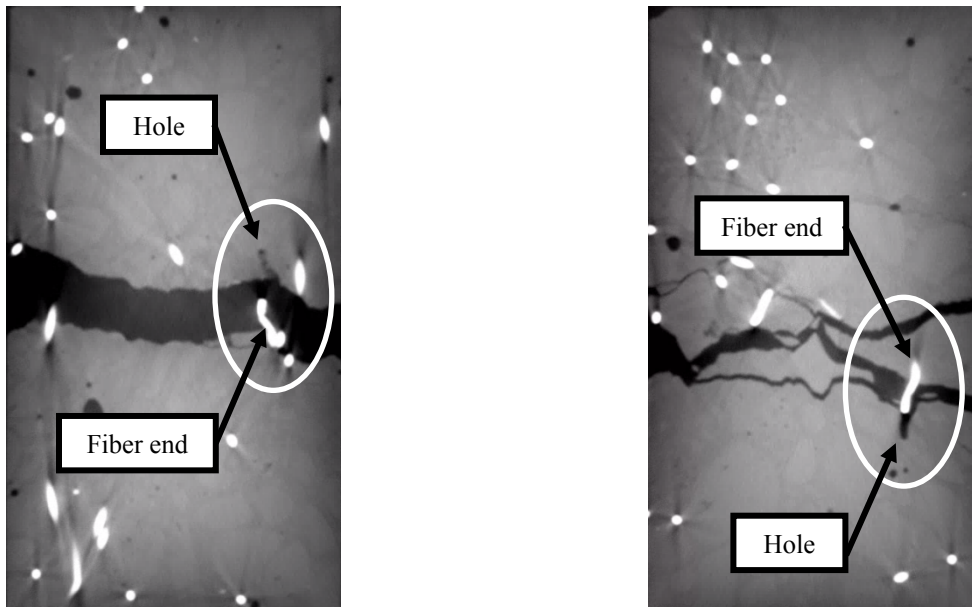
315

316 only on the mechanical properties of the fiber and in the second one, fiber, concrete matrix and the interface fiber-matrix
317 influence the behavior. Figures 13 to 18 show some slices, obtained through the CT-Scan, where these different failure
318 mechanisms can be observed for both series.



319

320 Figure 13: Two examples of cracked fibers from the R-Series (XY Section). On the left, the fiber crack occurs in the
321 middle of the fiber. On the right, the fiber crack occurs close to the end of the fiber.

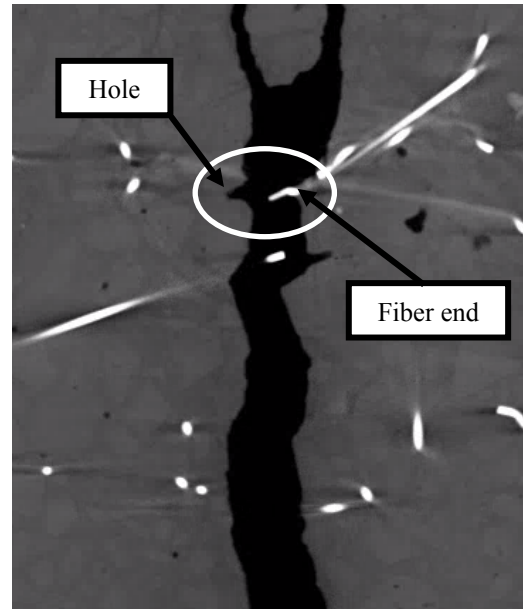
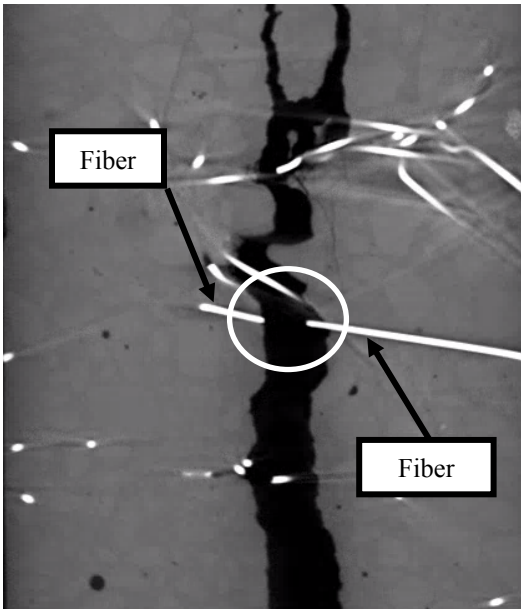


322

323 Figure 14: Two examples of fiber debonding from the R-Series (XY Section). On the left, fiber debonding in the
324 main crack. On the right, fiber debonding in a secondary crack.

325

326

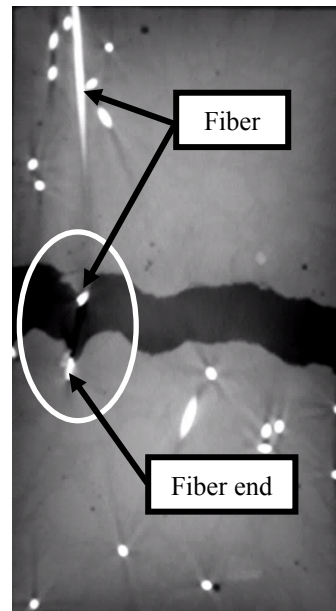
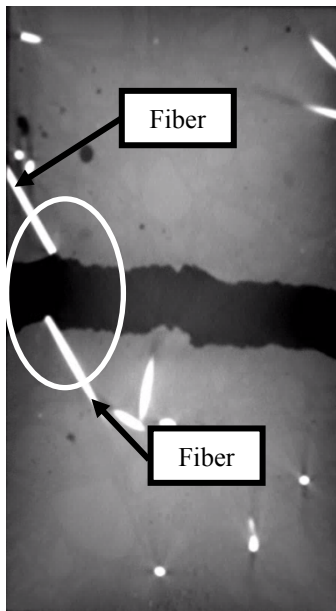


327

328

329

Figure 15: Two examples of crack failure from the R-Series (YZ Section). On the left, a cracked fiber. On the right, fiber debonding.

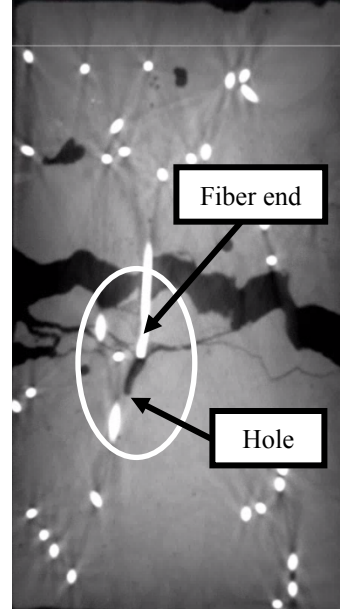
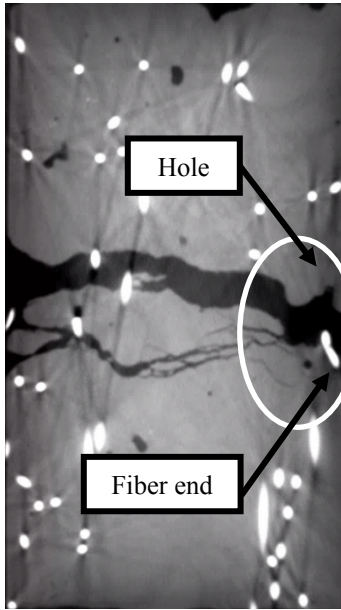


330

331

332

Figure 16: Two examples of cracked fibers from the M-Series (XY Section). On the left, a crack in the middle of the fiber. On the right, a crack close to the end of the fiber.



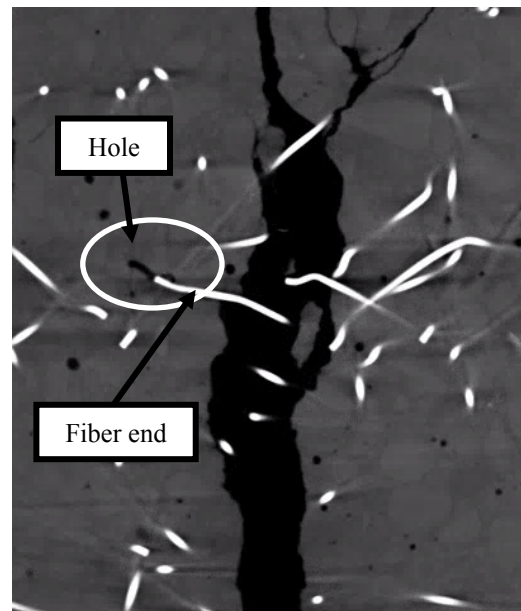
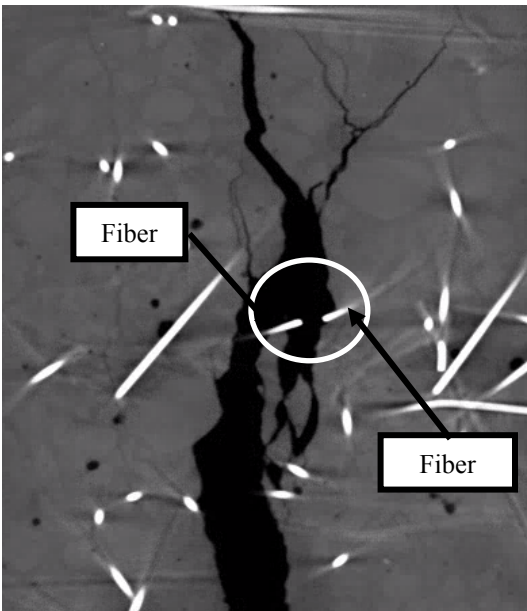
333

334

335

336

Figure 17: Two examples of fiber debonding from the M-Series (XY Section). On the left, fiber debonding in the main crack. On the right, fiber debonding in a secondary crack.



337

338

339

340

Figure 18: Two examples of crack failure from the M-Series (YZ Section). On the left, fiber cracking. On the right, fiber debonding.

341

342

343

The hooked-end fibers used in this work showed good anchoring. Cracks that cross the middle of the fiber tend to break **the fiber**. When the fiber orientation is perpendicular to the crack surface, the collapse is solely due to tensile forces. However, when the fiber is oblique to the crack surface, which occurs in most cases, the collapse is due to a combination of

344 axial, bending and shear. In this case, the failure directly depends on the tensile strength of the fiber material. Fiber cracking
345 can occur even when the crack crosses the fiber quite close to the fiber anchorage point, (Figures 13b and 14b).

346 On the contrary, when the crack crosses the fiber close to its end, the fiber tends to slip. Because of the shape of the
347 fiber anchorage, a complex stress field forms around the anchorage, which results in tensile stress and concrete cracking. In
348 this case, the failure mechanisms are more complex, as they depend on the fiber, the concrete matrix and the fiber-matrix
349 interface. Fiber debonding results in a hole in the back of the fiber. In this case, it can be observed that the distance between
350 the end of the fiber and the end of the hole provoked by fiber debonding coincides with the crack width.

351 Debonding is more common, i.e., most of the fibers fail because of slippage. The images provided by the CT-Scan
352 show that over 80% of the failures are due to debonding, while less than 20% are due to fiber breakage. This failure mechanism
353 shows a more plastic (post-peak) behavior. The conventional load vs debonding graph shows a linear increase up to a
354 maximum and then a progressive softening. [50-53]. On the contrary, fiber cracking occurs with far less displacement, i.e.,
355 with a much smaller crack opening. In consequence, it seems that the debonding mechanism is the one which provides the
356 post-peak softening behavior to the fiber-reinforced concrete specimens.

357 In addition, fibers were observed at some distance from the cracked concrete crack and, in consequence, undamaged.
358 This fact allows the “intact” fibers to be studied (Figure 19).

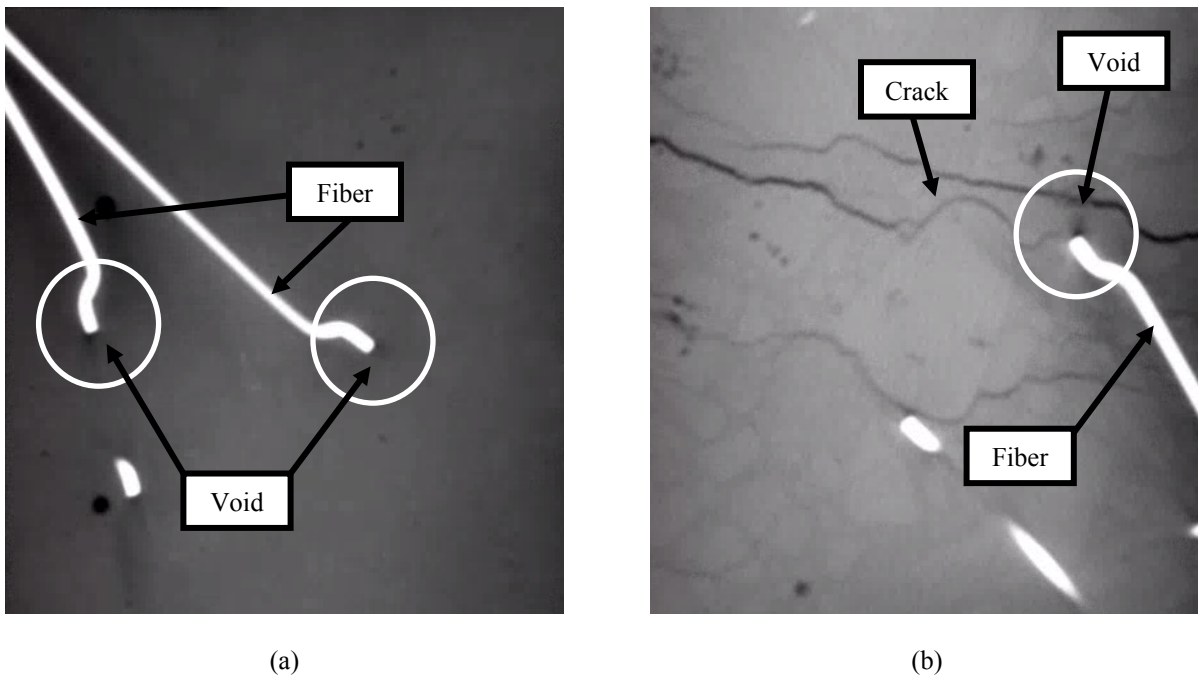


Figure 19: Voids at the end of the fibers (a) and crack initiation (b).

362 Small voids placed at the fiber end (Figure 19a) can be observed, which also facilitated the start of the cracks (Figure
363 19b). This fact indicates that the crack path tends to surround the fiber, resulting in debonding failure instead of breakage
364 failure.

365

366 **5. CONCLUSIONS**

367 In this work, the behavior under cyclic loading of two mixtures of steel-fiber-reinforced concrete has been studied.
368 Both mixtures had the same dosages and only differed in their fiber percentages. The R-Series contained 1% of fibers (by
369 volume), while the M-Series contained 2% of fibers. Prismatic specimens 150x150x600 mm were cast. The specimens were
370 subjected to a 3-point bending testing.

371 Based on the individual fatigue life of the specimens, the characteristic fatigue life has been estimated and compared
372 for both series. The specimens were subjected to a pre-defined damage level and then to a static test, after which their residual
373 tensile strength was measured.

374 In addition, once the specimen was tested and broken, a small sample was extracted from the surrounding of the crack
375 and scanned using a CT-Scan, in order to measure the fiber orientation.

376 The CT-Scan results showed very similar fiber orientations in both cases. The fibers were mainly oriented along the
377 horizontal plane. In the case of the R-Series, the fibers tended to be oriented along the longitudinal axis of the specimen, while
378 in the M-Series, the fibers showed no preferential orientation along the horizontal plane. However, the difference was not
379 very relevant between both series. In addition, the average fiber content that was measured was, in both cases, very close to
380 the expected content.

381 Regarding fatigue behavior, the results have shown that the S-N curves were substantially parallel in both cases. The
382 coefficient β , which represents the slope of the S-N curve, was almost identical in both mixtures. Hence, the fiber density had
383 no influence on the S-N curve. The fiber content modified the concrete tensile strength, but under the same maximum fatigue
384 stress level, the expected fatigue life was the same regardless of fiber content.

385 On the contrary, when the specimens were subjected to a cyclic test up to a pre-defined damage level (defined as the
386 quotient between the number of applied cycles and the fatigue life), and then subjected to a static test up to failure, the results
387 showed that the residual tensile strength strongly depended on fiber content. The M-Series (which showed the highest fiber
388 content) showed higher residual tensile strength values at every crack opening, and a lower loss of residual tensile strength
389 with the damage.

390 The CT-Scan has also provided information on the failure mechanisms. The results show that the debonding failure
391 mechanism was the most frequent, reaching more than 80% of total fiber failure. Only less than 20% of the failures were due

392 to fiber breakage. The failure due to the debonding of the fibers showed a more ductile behavior, while the failure due to
393 breakage of the fibers showed a less ductile behavior. In consequence, it appears that the debonding mechanism provided the
394 post-peak softening behavior in the fiber-reinforced concrete specimens.

395 The scans of the undamaged fibers revealed small voids at the end of the fibers, which also facilitated the initial crack
396 openings. This observation indicates that the crack path tended to surround the fiber, resulting in debonding failure instead of
397 breakage failure.

398

399 **6. ACKNOWLEDGEMENTS**

400 The authors are grateful for financial support from the Ministerio de Economía y Competitividad, BIA2015-68678-
401 C2-R, Spain.

402

403 **REFERENCES**

- 404 [1]. Zia, A.; Ali, M. (2017). "Behavior of fiber reinforced concrete for controlling the rate of cracking in canal-lining.
405 Construction and Building Materials, v 155, pp. 726-739.
- 406 [2]. Mazzoli, A.; Monosi, S.; Plescia, E.S. (2015). "Evaluation of the early-age-shrinkage of Fiber Reinforced Concrete
407 (FRC) using image analysis methods". Construction and Building Materials, v 101, pp: 596-601.
- 408 [3]. Ferrara, L.; Park, Y-D.; Shah, S.P. (2007). "A method for mix-design of fiber-reinforced self-compacting concrete".
409 Cement and Concrete Research, v 37, pp. 957-971.
- 410 [4]. Gonzalez, D.C.; Moradillo, R.; Mínguez, J.; Martínez, J.A.; Vicente, M.A. (2018). "Postcracking residual strengths of
411 fiber-reinforced high-performance concrete after cyclic loading". Structural Concrete, v 19(2), pp. 340-351.
- 412 [5]. Parvez, A.; Foster, S.J. (2015). "Fatigue Behavior of Steel-Fiber-Reinforced Concrete Beams". Journal of Structural
413 Engineering, v 141(4): 04014117: 1 to 8.
- 414 [6]. González, D.C.; Vicente, M.A.; Ahmad, S. (2015). "Effect of cyclic loading on the residual tensile strength of steel
415 fiber-reinforced high-strength concrete". Journal of Materials in Civil Engineering, v 27(9): 04014241: 1 to 8.
- 416 [7]. Zhang, J.; Stang, H.; Li, V.C. (1999). "Fatigue life prediction of fiber reinforced concrete under flexural load".
417 International Journal of Fatigue, v 21, pp. 1033-1049.
- 418 [8]. Mínguez, J.; González, D.C.; Vicente, M.A. (2018). "Fiber geometrical parameters of fiber-reinforced high strength
419 concrete and their influence on the residual post-peak flexural tensile strength". Construction and Building Materials,
420 v 168, pp. 906-922.

- 421 [9]. Bischoff, P.H. (2003). "Tension stiffening and cracking of steel fiber-reinforced concrete". *Journal of Materials in*
422 *Civil Engineering*, v 15(2), pp. 174-182.
- 423 [10]. Al Rikabi, F.T.; Sargand, S.M.; Khoury, I.; Hussein, H.H. (2018). "Material properties of synthetic fiber-reinforced
424 concrete under freeze-thaw conditions". *Journal of Materials in Civil Engineering*, v 30(6): 04018090, 1 to 13.
- 425 [11]. Niu, D.; Jiang, L.; Bai, M.; Miao, Y. (2013). "Study of the performance of steel fiber reinforced concrete to water and
426 salt freezing condition". *Materials and Design*, v 44, pp. 267-273.
- 427 [12]. Medeiros, A.; Zhang, X.; Ruiz, G.; Yu, R.C.; Velasco, M.S.L. (2015). "Effect of the loading frequency on the
428 compressive fatigue behavior of plain and fiber reinforced concrete". *International Journal of Fatigue*, v 70, pp. 342-
429 350.
- 430 [13]. Poveda, E.; Ruiz, G.; Cifuentes, H.; Yu, R.C.; Zhang, X. (2017). "Influence of the fiber content on the compressive
431 low-cycle 585 fatigue behavior of self-compacting SFRC". *International Journal of Fatigue*, v 101, pp. 9-17.
- 432 [14]. Goel, S.; Singh, S.P.; Singh, P. (2012). "Flexural fatigue strength and failure probability of Self Compacting Fibre
433 Reinforced Concrete beams". *Engineering Structures*, v 40, pp. 131-140.
- 434 [15]. Singh, S.P.; Sharma, U.K. (2007). "Flexural fatigue strength of steel fibrous concrete beams". *Advances in Structural*
435 *Engineering*, v 40(2), pp. 197-207.
- 436 [16]. Singh, S.P., Mohammadi, Y.; Kaushik, S.K. (2005). "Flexural fatigue analysis of steel fibrous concrete containing
437 mixed fibers". *ACI Materials Journal*, v 102(6), pp. 438-444.
- 438 [17]. Bajaj, V.; Singh, S.P.; Singh, A.P. et al (2012). "Flexural fatigue analysis of hybrid fibre-reinforced concrete".
439 *Magazine of Concrete Research*, v 64(4), pp. 361-373.
- 440 [18]. Mohammadi, Y.; Kaushik, S.K. (2005) "Flexural fatigue-life distributions of plain and fibrous concrete at various
441 stress levels". *Journal of Materials in Civil Engineering*, v 17(6), pp. 650-658.
- 442 [19]. Singh, S.P.; Kaushik, S.K. (2001). "Flexural fatigue analysis of steel fiber-reinforced concrete". *ACI Materials Journal*,
443 v 98(4), pp 306-312.
- 444 [20]. Plizzari, G.A.; Cangianno, S.; Cere, N. (2000). "Postpeak behavior of fiber-reinforced concrete under cyclic tensile
445 loads". *ACI Materials Journal*, v 97(2), pp. 182-192.
- 446 [21]. Graeff, A.G.; Pilakoutas, K.; Neocleous, K., et al (2012) "Fatigue resistance and cracking mechanism of concrete
447 pavement reinforced with recycled steel fibres recovered from post-consumer tyres". *Engineering Structures*, v 45, pp.
448 385-395.
- 449 [22]. Li, H.; Zhang, M.; Ou, J. (2007). "Flexural fatigue performance of concrete containing nano-particles for pavement".
450 *International Journal of Fatigue*, v 29(7), pp. 1292-1301.

- 451 [23]. Patel, P.A.; Desai, A.K.; Desai, J.A. (2013) "Evaluation of RC and SFRC exterior beam-column joint under cyclic
452 loading for reduction in lateral reinforcement of the joint region". Magazine of Concrete Research, v 65(7), pp. 405-
453 414.
- 454 [24]. Zhang, Y.; Harries, K.A.; Yuan, W. (2013). "Experimental and numerical investigation of the seismic performance of
455 hollow rectangular bridge piers constructed with and without steel fiber reinforced concrete". Engineering Structures,
456 v 58, pp. 255-265.
- 457 [25]. Shah A.; Abid, Ribakov Y. (2011) "Recent trends in steel fiber high-strength concrete". Materials and Design, v 32,
458 pp. 4122-4151.
- 459 [26]. Banjara, N.K.; Ramanjaneyulu, K. (2018). "Experimental Investigations and Numerical Simulations on the Flexural
460 Fatigue Behavior of Plain and Fiber-Reinforced Concrete". Journal of Materials in Civil Engineering, v. 30(8):
461 04018151, 1 to 15.
- 462 [27]. Johnston, C.D.; Zemp, R.W. (1991). "Flexural Fatigue Performance of Steel Fiber Reinforced Concrete – Influence of
463 Fiber Content, Aspect Ratio and Type". ACI Materials Journal, n° 88-M44, pp. 374-383.
- 464 [28]. Bernardo, H.; Vicente, M.A.; González, D.C.; Martínez, J.F. (2015). "Efecto de las cargas cíclicas sobre la adherencia
465 hormigón-acero en hormigones sumergidos". Hormigón y Acero, v 66(276), pp. 225-236.
- 466 [29]. Vicente, M.A.; González, D.C.; Mínguez, J.; Martínez, J.A. (2014). "Residual modulus of elasticity and maximum
467 compressive strain in HSC and FRHSC after high-stress-level cyclic loading". Structural Concrete, v. 15(2), pp. 210-
468 218.
- 469 [30]. Bernardo, H.; Vicente, M.A.; González, D.C.; Martínez, J.F. (2014). "Cyclic bond testing of steel bars in high-
470 performance underwater concrete". Structural Engineering International, v 24(1), pp. 37-44.
- 471 [31]. Vicente, M.A.; González, D.C.; Martínez, J.A. (2014). "Mechanical Response of Partially Prestressed Precast Concrete
472 I-Beams after High-Range Cyclic Loading." Pract. Period. Struct. Des. Constr., 10.1061/(ASCE)SC.1943-
473 5576.0000225, 04014022.
- 474 [32]. Urban, S.; Strauss, A.; Macho, W.; Bergmeister, K.; Dehlinger, C. and Reiterer, M. "Zyklisch belastete
475 Betonstrukturen. Robustheits- und Redundanzbetrachtungen zur Optimierung der Restnutzungsdauer (Concrete
476 structures under cyclic loading. Robustness and redundancy considerations for residual lifetime optimization) (In
477 German)". Bautechnik, vol. 89, no 11, 2012,
- 478 [33]. Zanuy, C.; Albajar, L.; De la Fuente P. (2011). "The fatigue process of concrete and its structural influence," Materiales
479 de Construcción, v 61(303), pp. 385-399.

- 480 [34]. Zanuy, C.; Albajar, L.; de la Fuente, P. (2009). "Sectional analysis of concrete structures under fatigue loading", *ACI*
481 *Struct. J.*, v 106(5), pp. 667-677.
- 482 [35]. Zhang, B.; Wu, K. (1997). "Residual fatigue strength and stiffness of ordinary concrete under bending" *Cement and*
483 *Concrete Research*, v 27(1), pp. 115-126.
- 484 [36]. International Federation for Structural Concrete. (2010). "Model code for concrete structures." *FIB Bulletin 65*,
485 Lausanne, Switzerland.
- 486 [37]. Vicente, M.A.; Ruiz, G.; González, D.C.; Mínguez, J.; Tarifa, M.; Zhang, X. (2018). "CT-Scan study of crack patterns
487 of fiber-reinforced concrete loaded monotonically and under low-cycle fatigue". *International Journal of Fatigue*, v.
488 114, pp. 138-147.
- 489 [38]. Balazs, G.L.; Czoboly, O.; Lubloy, E.; Kapitany, K.; Barsi, A. (2017). "Observation of steel fibers in concrete with
490 computed tomography". *Construction and Building Materials*, v. 140, pp. 534-541.
- 491 [39]. Pastorelli, E.; Herrmann, H. (2016). "Time-efficient automated analysis for fibre orientations in steel fibre reinforced
492 concrete". *Proceedings of the Estonian Academy of Sciences*, v 65 (1), pp. 28-36.
- 493 [40]. Herrmann, H.; Pastorelli, E.; Kallonen, A.; Suuronen, J.P. (2016). "Methods for fibre orientation analysis of X-ray
494 tomography images of steel fibre reinforced concrete (SFRC)". *Journal of Materials Science*, v 51(8), pp. 3772-3783.
- 495 [41]. Ponikiewski, T.; Katzer, J. (2016). "X-ray computed tomography of fibre reinforced self-compacting concrete as a tool
496 of assessing its flexural behaviour". *Materials and Structures*, v. 49, pp. 2131-2140.
- 497 [42]. Ponikiewski, T.; Katzer, J.; Bugdol, M.; Rudzki, M. (2014). "Determination of 3D porosity in steel fibre reinforced
498 SCC beams using X-ray computed tomography". *Construction and Building Materials*, v 68, pp. 333-340.
- 499 [43]. Vicente, M.A.; González, D.C.; Mínguez, J. (2014). "Determination of dominant fibre orientations in fibre-reinforced
500 high strength concrete elements based on computed tomography scans". *Nondestructive Testing and Evaluation*, v
501 29(2), pp. 164-182.
- 502 [44]. Vicente, M.A.; Mínguez, J.; González, D.C. (2017). "The use of computed tomography to explore the microstructure
503 of materials in civil engineering: from rocks to concrete". In: Halefoglu Ahmet Mesrur, editor. *Computed tomography*
504 *- advanced applications*. InTech.
- 505 [45]. European Committee for Standardization (2004). "EUROCODE 2, Design of concrete structures". *Eurocode2*,
506 Brussels, Belgium.
- 507 [46]. Aas-Jakobsen, K. (1970). "Fatigue of concrete beams and columns." *Institutt for betonkonstruksjoner*, NTH
508 Trondheim, Trondheim, Norway, 148.
- 509 [47]. Hsu, T.T.C. (1981). "Fatigue of plain concrete." *ACI Journal of Materials*, v. 78, pp. 292-305.

- 510 [48]. Tepfers, R. (1979). "Tensile fatigue strength of plain concrete." *ACI Journal*, v. 76, pp. 919–933.
- 511 [49]. Oh, B.H. (1986). "Fatigue analysis of plain concrete in flexure". *Journal of Structural Engineering*, v. 112:2, pp. 306–
512 312.
- 513 [50]. Bhutta, A.; Farooq, M.; Borges, P.H.R.; Banthia, N. (2018). "Influence of fiber inclination angle on bond-slip behavior
514 of different alkali activated composites under dynamic and quasi-static loadings". *Cement and Concrete Research*, v.
515 107, pp. 236-246.
- 516 [51]. Wu, Z.; Khayat, K.H.; Shi, C. (2018). "How do fiber shape and matrix composition affect fiber pullout behavior and
517 flexural properties of UHPC?" *Cement and Concrete Composites*, v. 90, pp. 193-201.
- 518 [52]. Lee, S.F.; Jacobsen, S. (2011). "Study of interfacial microstructure, fracture energy, compressive energy and
519 debonding load of steel fiber-reinforced mortar". *Materials and Structures*, v. 44 (8), pp. 1451–1465.
- 520 [53]. Wille, K.; Naaman, A.E. (2012). "Pullout behavior of high-strength steel fiber embedded in ultra-high-performance
521 concrete" *ACI Journal of Materials*, v. 109 (4), pp. 479–487.

Main highlights.

1. This work show the influence of the fiber content and fiber orientation on the fatigue behavior of concrete specimens.
2. The computed tomography (CT) scan technology becomes a powerful technology to study the internal microstructure.
3. The fiber content modified the concrete tensile strength, but under the same maximum fatigue stress level, the expected fatigue life was the same regardless of fiber content.
4. The CT-Scan has also provided information on the failure mechanisms. The results show that the debonding failure mechanism was the most frequent.

1 **COMPUTED TOMOGRAPHY SCANNING OF THE INTERNAL MICROSTRUCTURE, CRACK**
2 **MECHANISMS, AND STRUCTURAL BEHAVIOR OF FIBER-REINFORCED CONCRETE UNDER STATIC**
3 **AND CYCLIC BENDING TESTS**

4
5 Miguel A. Vicente^{1,2,*}, Jesús Mínguez¹, Dorys C. González^{1,2}.

6
7 ¹ Department of Civil Engineering, University of Burgos, c/ Villadiego, s/n, 09001, Burgos (Spain).

8 ² Department of Civil Engineering, Parks College of Engineering, Aviation and Technology, Saint Louis University, 3540
9 Lindell Blvd, Saint Louis, MO (USA).

10
11 * Corresponding Author: mvicente@ubu.es

12
13 Number of words: 5193

14 Number of tables and figures: 23

15
16 Keywords: fatigue, high strength concrete, fibre-reinforced concrete, residual tensile strength, CT-Scan technology.

19 **ABSTRACT**

20 Fiber-reinforced concrete (FRC), its behavior, and the effects of cyclic loading on its internal microstructure are studied
21 in this paper. Particular attention is given to the evolution of the residual tensile strength of the fiber-reinforced concretes and
22 damage following cyclic flexural loading. A numerical equation is also proposed to estimate the residual tensile strength,
23 depending on crack width, damage, fiber content, and fiber orientation. A total of 65 prismatic specimens, in two different
24 series, were tested: one designed with 1% of fibers by volume and the other with 2% of fibers. The specimens were not
25 notched, but had previously been subjected to pre-cracking, which has a similar effect to notching, although the specimens
26 become more vulnerable to fatigue. Both fiber content and fiber orientation were measured using computed tomography (CT)
27 scans. The results showed that the damage provoked a progressive reduction in the residual tensile strength. The differences
28 in the behavior of both series were mainly related to their fiber content and, to a lesser extent, to their fiber orientation.

29
30 **1. INTRODUCTION**

31 Fiber-Reinforced Concrete (FRC) is an increasingly widespread technical solution in civil engineering. It is a very
32 suggestive solution because of the reduction of the labor cost, especially if it is combined with self-compacting concrete. In
33 most cases, the addition of fibers improves the mechanical behavior of concrete: less cracking [1-3], improved fatigue life [4-
34 7], increased maximum tensile strength [8, 9], improved freeze-thaw behaviour [10, 11], and extended fatigue life [12, 13].

35 Fatigue in concrete may be understood as a process of mechanical weakening until failure. Cyclic loading causes the
36 emergence of microcracks and their enlargement inside the concrete mass, around internal defects, such as voids, etc. The
37 macroscopic consequences of fatigue are progressive changes in the mechanical parameters of the concrete.

38 Most research over recent years has focused on fatigue life, i.e., the number of loading cycles that the concrete element
39 can withstand, and the S-N curves, which correlate with the stress level and the fatigue life [14-25]. However, only very few
40 research works have focused on the mechanical parameters of concrete and their modification under cyclic loading [4, 6, 26-
41 35].

42 The weakening of FRC can be defined by changes in the residual tensile strength, $f_{R,i}$, following a number of cycles,
43 which is taken into account in the design of FRC structures. According to the Model Code 2010 [36], the structural design of
44 the FRC is based on the residual stress provided by the reinforcing fibres. In particular, the values of $f_{R,1}$ and $f_{R,3}$ are used in
45 the formulation, defined as the residual strength values associated with crack openings from 0.5 to 2.5 mm, respectively. In
46 the case of structural elements subjected to cyclic loading over time, a progressive decrease in the residual tensile strength is
47 expected [4, 6, 26], the minimum values of which are parameters to prevent unsafe designs.

48 Both the fatigue life and the loss of residual tensile strength strongly depend on the geometrical and mechanical
49 characteristics of the fibers (shape, length, slenderness, etc.), the number of fibers and fiber distribution and orientation within
50 the concrete matrix.

51 Regarding fiber distribution and orientation, Computed Tomography (CT) Scan technology is a powerful tool to study
52 the internal microstructure of the matter, and particularly, to study fiber distribution and orientation in the case of FRC. CT is
53 a non-destructive technique used to visualize the internal microstructure of materials based on the properties of X-rays. A CT-
54 Scan facility contains an intensity-controlled X-ray source and a detector, which measures the loss of X-ray intensity. During
55 the scanning process, the X-rays are emitted and the detector measures and records the final X-ray intensity for all the X-rays.
56 By rotating the specimens, a lot of different relative directions across the specimen are applied and, finally, every point of the
57 sample is traversed by different X-rays, from different directions.

58 During the post-scan data processing, the density at each point of the sample is obtained in accordance with the
59 measured loss of X-ray intensity for all the X-rays, since there is a relation between the loss of X-ray intensity and the density
60 of the matter that it passes through. The result is a 3D grey-scale image composed of voxels (ranging from 0 to 255), where
61 the grey value corresponds to the density of the voxel. Clear grey tones correspond to high densities while dark grey tones
62 correspond to low densities.

63 Beyond its traditional use in medicine, this technology is currently widely used in concrete research, especially in
64 fiber-reinforced concrete [37-43]. The enormous advantage of CT-Scan technology is that it permits the exact position, and
65 orientation of each individual fiber to be measured, which is otherwise impossible with other techniques. Moreover, the
66 combined use of CT-Scan technology with a macroscopic test is currently providing interesting results, since it is possible to
67 correlate the internal microstructure with the macroscopic response. A detailed explanation of CT-Scan technology and its
68 use in several engineering fields can be obtained in [44].

69 The aim of this research is to analyze how fiber content and fiber orientation influence fatigue life and residual tensile
70 strength in fiber-reinforced concrete specimens that have undergone static and cyclic three-point bending tests. Having ended
71 the cyclic loading test, the specimens were subjected to static testing until failure, and then their post-cracking residual
72 strengths were measured. The procedure developed by Gonzalez and co-workers [4, 6] was used.

73 The structure of this paper will be as follows: The experimental program will be presented in Section 2, the
74 experimental results will be described and discussed in Section 3, the failure mechanisms will be described in Section 4, and
75 finally, the conclusions will be presented in Section 5.

76

77 **2. EXPERIMENTAL PROGRAM**

78 In this section, the materials, the testing procedure and the scanning procedure will be described.

79 2.1 Materials

80 The whole test campaign had 65 prismatic specimens, belonging to two series: labelled R-Series and M-Series. In both
81 cases, the cement paste was the same and the only difference was the fiber content, which was 1% by volume in the R-Series
82 and 2% by volume in the M-Series (Table 1).

84 Table 1: Mix proportions

Materials	R-Series	M-Series
Cement (kg/m ³)	400	
Water (kg/m ³)	125	
Superplasticizer (kg/m ³)	14	
Silica fume (kg/m ³)	6	
Fine aggregate (kg/m ³)	800	
Coarse aggregate (kg/m ³)	1,080	
Fiber (% by volume)	1%	2%

85
86 Ordinary Portland cement, crushed limestone coarse and fine aggregates (maximum size 15 mm) were used. Hook-
87 end steel fibres of 50 mm in length and 1.0 mm in diameter were incorporated in the concrete, together with superplasticizer
88 Glenium 52 BASF and nanosilica MEYCO MS685 BASF additives. The concrete quality as per Eurocode 2 was C70/85 [45].
89 The specimens were cured for 180 days in a curing room at both a constant relative humidity of 100% and an ambient
90 temperature of 20°C. The specimens were then removed from the curing room and held under laboratory conditions until
91 testing. All the specimens were, at least, 300 days-old when the testing campaign began. So, the possible strength increase
92 during the fatigue test was minimized. The 28-day average compressive strength of the mixture was 81.5 MPa for the R-
93 Series and 78.1 MPa for the M-Series, with a standard deviation of 4.3 MPa.

94 A total of 40 R-Series prisms and 25 M-Series prisms were prepared. In all cases, the prism dimensions were 600 mm
95 in length, 150 mm in width and 150 mm in height. In addition, two sets of cylinders with a diameter of 150 mm and a height
96 of 300 mm were cast for further characterization of the concrete (mainly to obtain the compressive strength).

98 2.2 Testing procedure

99 The testing procedure for both series is well described in [4, 6]. In summary, the test program included the 4 phases
100 described as follows (Figure 1):

- 101 1. Phase 1: Initial crack. During the first phase, all the prismatic specimens were subjected to a three-point static
102 bending test until small cracks appeared. In this first phase, forty R-Series specimens and twenty-five M-Series
103 specimens were tested. The midspan cross-section of the specimens was not notched.
- 104 2. Phase 2: Fatigue tests. In the second phase, some specimens were subjected to a three-point cyclic bending test
105 to failure, in order to obtain the characteristic fatigue life of the material. In this second phase, twelve specimens
106 of the R-Series were tested, and nine specimens of the M-Series.
- 107 3. Phase 3: Cyclic tests. In the third phase, other specimens underwent a three-point cyclic bending test up to a
108 preset number of load cycles, with the aim of inducing controlled fatigue damage in the specimens. In this third
109 phase, twenty-one R-Series specimens and twelve M-Series specimens were tested
- 110 4. Phase 4: Static tests. In the last phase, all the specimens tested in the third phase plus the pre-cracked ones not
111 subjected to the cyclic tests underwent to a three-point static bending test. In this way, variations in the residual
112 tensile strength in relation to fatigue damage could be detected. In this fourth phase, twenty-eight specimens of
113 the R-Series were tested, and sixteen specimens of the M-Series.

114

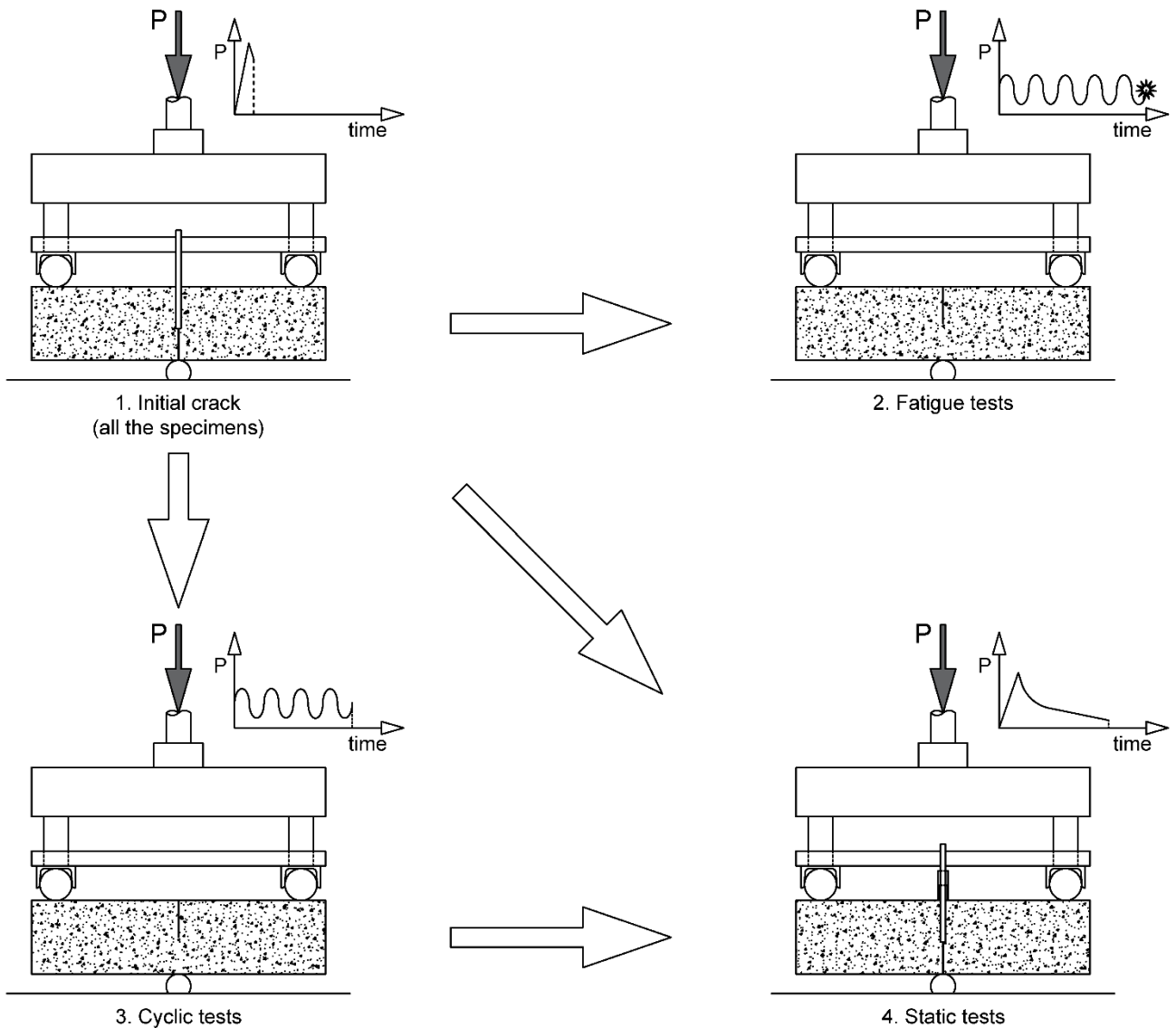


Figure 1: Explanation of the four test phases [4].

115

116

117 2.3 CT-Scan test

118 Additionally, computed tomography (CT) scans were performed to visualize the internal microstructure of concrete
 119 for further study. This technology permits a close examination of the fiber locations and orientations of each specimen. The
 120 fiber content has been directly taken from the mix dosage.

121 In this study, concrete specimens were CT-scanned by a GE Phoenix v|tome|x device equipped with a tube of 300
 122 kV/500W. The entire specimen was not scanned, but only a part of it, extracted from the central region, surrounding the crack
 123 (Figure 2). The scanning sample was 150 mm in height, 100 mm in width, and 50 mm in thickness.

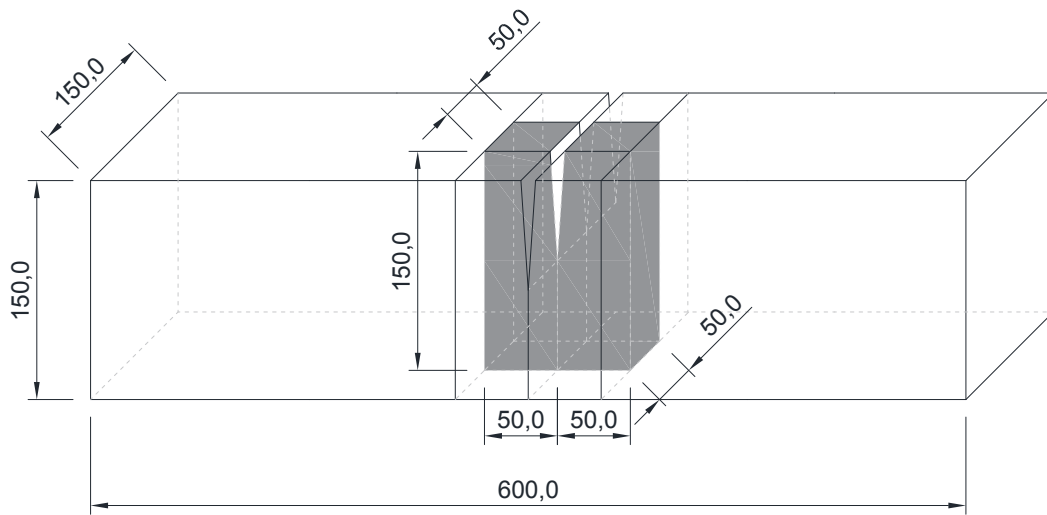


Figure 2: Location of the scanned piece from the whole prism.

124

125

126

127

This portion of the prism provides the most valuable information, since the fibers bridging the crack are the ones which control the cracking process.

128

129

Using a post-processing software, a total of 2,500 2D slices of 2048x2048 pixels (Figure 3) were obtained throughout the height of the specimen from the CT-scan machine. In this case, the horizontal resolution was $60 \times 60 \mu\text{m}^2$ and the vertical distance between the slices was $60 \mu\text{m}$ for a section with a diagonal length of 111.8 mm. After that a 3D image of the whole specimen was generated using all the above-mentioned 2D images. The post-processing software assigns a grey value to each voxel (volumetric pixel), coded as integer numbers between 0 and 255, where 0 equals black and 255 equals white. A value of 255 is assigned to the densest voxel and a value of 0 is assigned to the least dense voxel. For the rest of the voxels a linear relation is considered. The conclusion of the scanning process is a file including X, Y, and Z Cartesian coordinates of the voxel center of gravity and an integer number, from 0 to 255, regarding the density. The total number of voxels in a specimen was around $3.5 \cdot 10^9$.

137

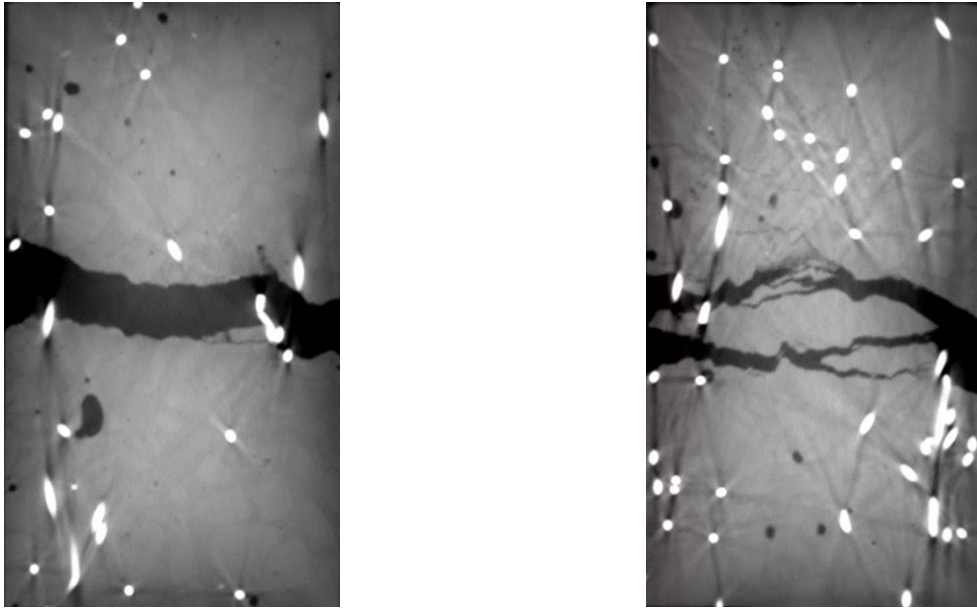


Figure 3: Slices belonging to different mixtures. From left to right: R-Series and M-Series.

The next step in this process is to identify and isolate each individual fiber inside the specimen with image analysis software. First of all, the software identifies the voxels belonging to voids, which show a range of grey values. In this case, once the histogram of grey scale is studied, the considered range for fibers was between 200 and 255 (Figure 4).

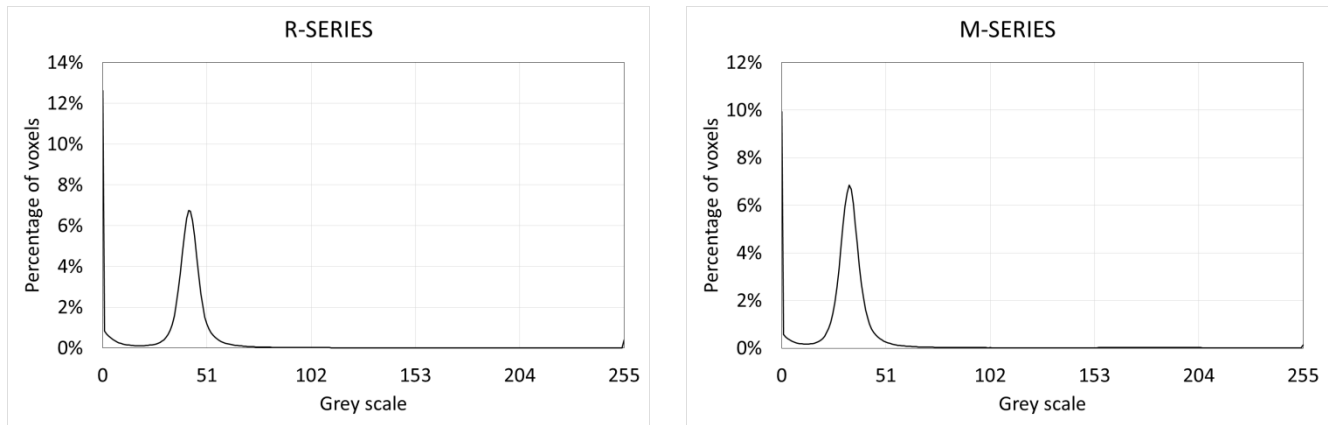
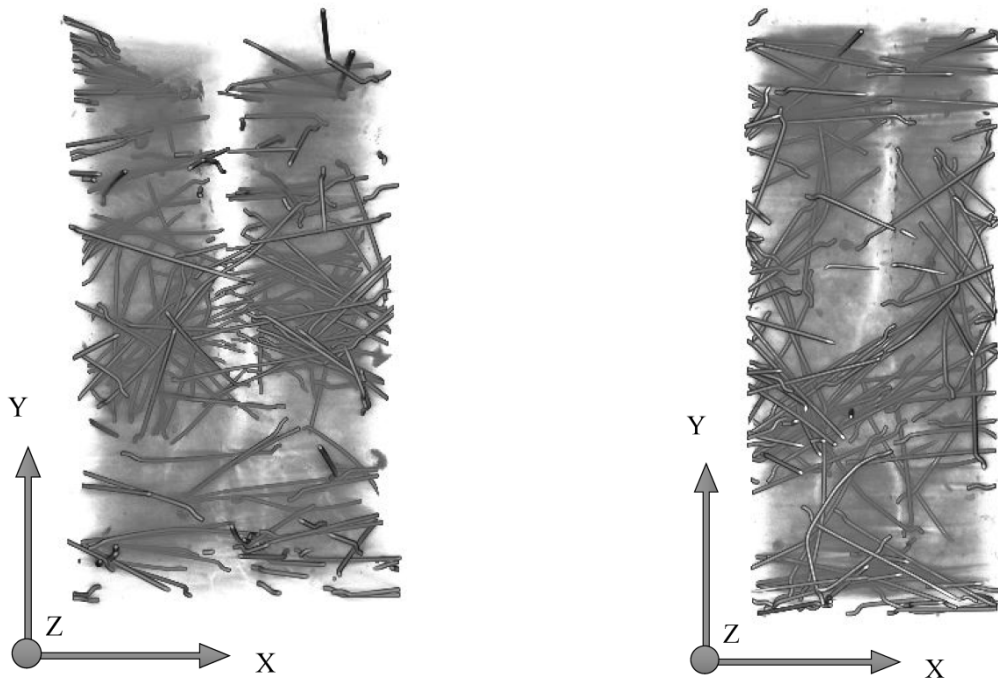


Figure 4: Histograms of grey scale.

Then, all the voxels in contact are merged, which come from the same fibers. The software identifies and isolates the different fibers. (Figure 5).



149

150

Figure 5: 3D views of the specimen belonging to different series. From left to right: R-Series and M-Series.

151

152

153

154

155

156

The final result of this image analysis is a dot matrix containing the Cartesian coordinates X, Y, and Z of the center of gravity of each fiber, the fiber length, and the orientation according to the Cartesian axis. In this case, the x-axis is transversal, the y-axis is longitudinal, and the z-axis is the vertical. The fiber orientation along the longitudinal axis is of interest, since it is related to the bridging of the crack. Figure 6 shows an isometric view of the fibers in a specimen from each series.

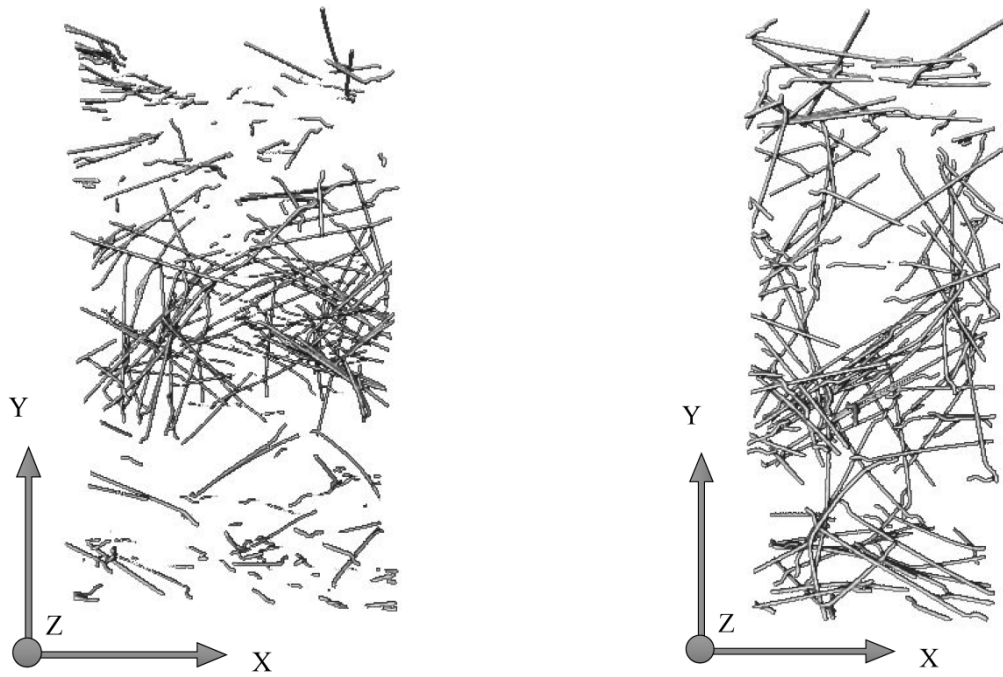


Figure 6: 3D views of the fibers belonging to different series. From left to right: R-Series and M-Series.

The CT-Scan device provides an enormous amount of useful information. However, it is not possible to obtain conclusions through direct observation of the 3D images alone. The data has to be post-processed using Digital Image Processing (DIP) software and/or post-processing sub-routines.

3. EXPERIMENTAL RESULTS

In this section, both the results of the CT-Scan and the results of the fatigue tests and the static post-cyclic tests will be presented. Finally, both the results from the CT-Scan and from the mechanical test will be correlated with each other.

3.1 CT-Scan analysis

Direct observation of the 3D images to distinguish the differences between both series is insufficient, and all the more so, for their quantification. In this case, the visualization and analysis software, AVIZO (FEI Visualization Sciences Group, Hillsboro, Oregon, USA), in combination with some sub-routines devised for the test were used to analyse the large data sets from the CT-Scan. The values shown in the different tables and figures refer to the average values of the specimens belonging to the same series.

174 3.1.1 Fiber content

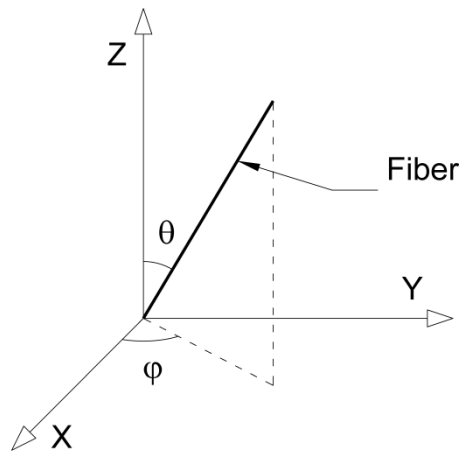
175 Using the CT-scan data on the full length of each individual fiber, the exact length of the fiber inside the scanned
176 sample can be computed. The total fiber volume may be obtained by multiplying this value by the section of the fiber. The
177 fiber content is defined as the quotient between the total fiber volume and the total volume of the sample.

178 In this case, the average fiber volumes were 0.98% for the R-Series and 1.97% for the M-Series. These values coincide
179 with the theoretical ones.

180

181 3.1.2 Fiber orientation

182 Fiber orientation is the most important result regarding the CT-Scan analysis. The primary angular information
183 provided by AVIZO are the values of both θ (theta) and ϕ (phi) (Figure 7). Theta is a polar angle, i.e., the angle between the
184 main axis of the fiber (the one containing its length) and the Z axis. Phi is the azimuthal angle, i.e., the angle between the
185 projection of the main axis on the XY plane and the X axis. Theta varies from 0° to 90° while phi varies from -90° to 90° .



186

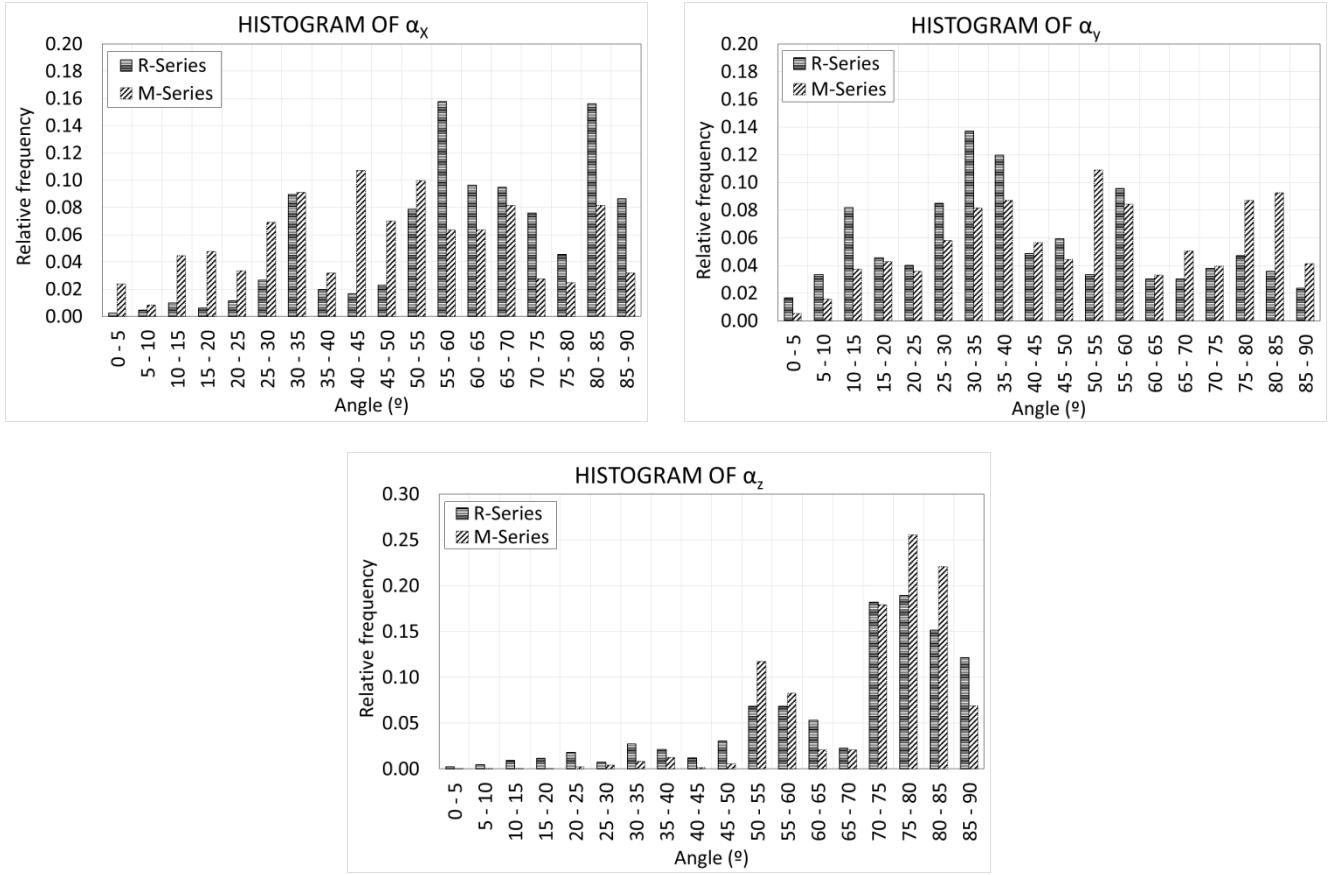
187 Figure 7: Identification of θ (theta) and ϕ (phi) angles

188 The angles according the Cartesian axis α_x , α_y and α_z can be obtained by the following expression (eq. 1):

$$\begin{aligned}\alpha_x &= \text{acos}[\sin(\theta) \cdot \cos(\phi)] \\ \alpha_y &= \text{acos}[\sin(\theta) \cdot \sin(\phi)] \\ \alpha_z &= \theta\end{aligned}\tag{1}$$

189 Next, the average histograms of angle distribution are shown, for both series (Figure 8).

190



191

192

Figure 8: Histograms of fiber orientation by Cartesian axis

193

194 In both cases, it is clearly observed that fibers are horizontally oriented, i.e., perpendicular to the z-axis, as the
 195 histogram of α_z shows that most of the fibers have an angle close to 90° . Regarding the x- and the y-axis of the M-Series, it
 196 appears that the fibers are randomly distributed along both axes. On the contrary, in the case of the R-Series, the fibers appear
 197 to show a slight tendency to remain parallel to the y-axis, since the histogram of α_x reveals that most of the fibers show an
 198 obtuse angle greater than 45° and the histogram of α_y reveals that most of the fibers show an acute angle under 45° .

199 The efficiency index (e_i) defines the numerical orientation along the x-, y- and z-axes by the following equation [43]

200 (eq. 2):

$$e_{i_x} = \sum_{i=1}^n f_{x,i} \cdot \cos(\bar{\alpha}_{x,i})$$

$$e_{i_y} = \sum_{i=1}^n f_{y,i} \cdot \cos(\bar{\alpha}_{y,i})$$

(2)

$$ei_z = \sum_{i=1}^n f_{z,i} \cdot \cos(\bar{\alpha}_{z,i})$$

201

202

where, $f_{x,i}$, $f_{y,i}$ and $f_{z,i}$ are the relative frequencies of each histogram bar, and $\bar{\alpha}_{x,i}$, $\bar{\alpha}_{y,i}$ and $\bar{\alpha}_{z,i}$ are the average values of the angles of each histogram bar. The efficiency index can show values from 0 to 1, where 0 means that all the fibers are oriented perpendicularly to the Z axis and 1 means that all the fibers are oriented parallel to the Z axis.

203

204

205

Table 2 shows the average values of the efficiency index of fibers for all series. In addition, the values in brackets represent the standard deviation.

206

207

208

Table 2: Efficiency index.

Series	ei_x	ei_y	ei_z
R-Series	0.44 [0.07]	0.70 [0.12]	0.35 [0.05]
M-Series	0.62 [0.11]	0.58 [0.10]	0.30 [0.05]

209

210

Observing the histograms in Figure 7, the R-Series shows a higher efficiency index along the y-axis, which means that the fibers tend to be oriented along the longitudinal axis. On the contrary, the M-Series shows that both ei_x and ei_y are quite similar, which means that the fibers are uniformly distributed along the XY plane. Regarding the z-axis, in both cases the value of ei_z is quite small, which means that the fibers tend to be oriented perpendicular to the z-axis, i.e., on the horizontal plane. Both series show a similar value of ei_z , so no relevant differences between them can be observed regarding this parameter.

211

212

213

214

215

216

As explained before, the most interesting efficiency index is ei_y , which represents the orientation of the fibers along the longitudinal axis, i.e., along the orthogonal direction to the crack surface.

217

218

219

3.1 Fatigue testings

220

Twelve prismatic specimens of the R-Series and nine prismatic specimens of the M-Series were tested under three-point cyclic bending tests up until fatigue failure. In all cases, no specimen had been pre-notched, but the specimens had been pre-cracked in a static three-point bending test until the first crack appeared. The previous damage significantly reduced the fatigue life [6].

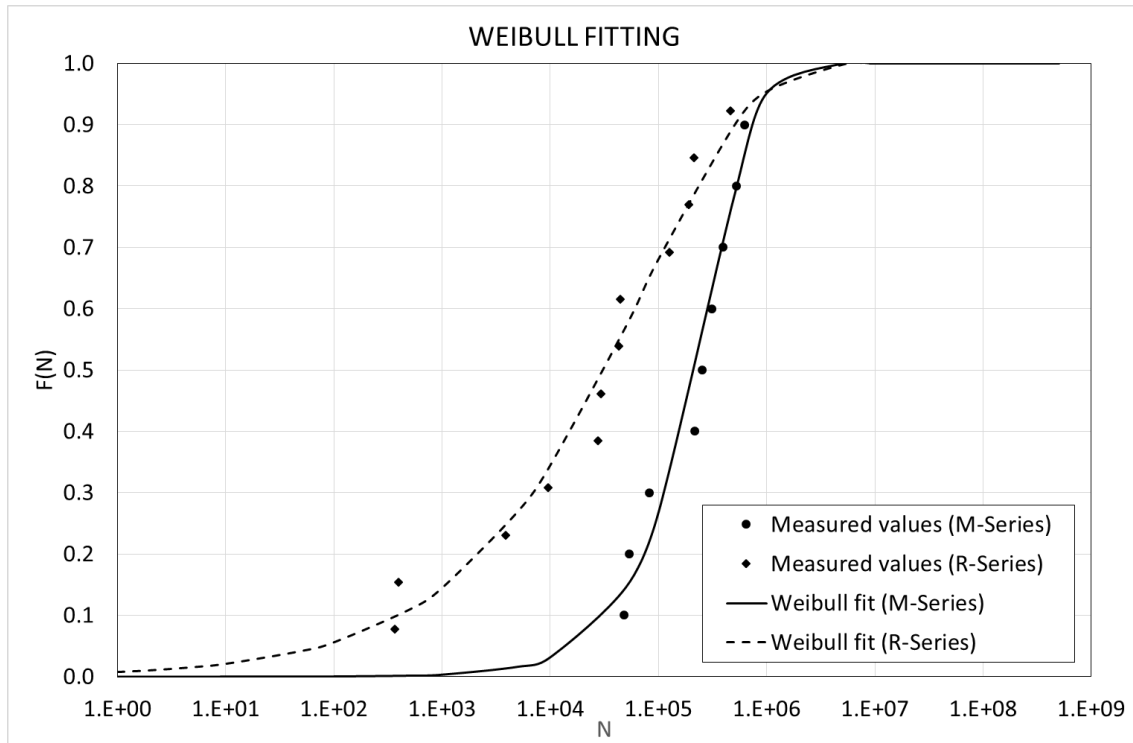
221

222

223

224 In the case of the R-Series, the cyclic load applied to each specimen ranged from 65% to 5% of its residual (or final)
 225 bending strength (obtained during the initial precracking test). In the case of the M-Series, the cyclic load ranged from 60%
 226 to 15% of its residual bending strength. The fatigue life of each series can be found in [4, 6].

227 By fitting the values to the Weibull distribution, the fatigue life of the different failure probabilities can be found for
 228 both series (Figure 9). In both cases, the representative fatigue life, N_{cr} , is defined as the number of cycles, N , corresponding
 229 to a failure probability of 20% ($P_f = 0.20$) (Table 5).



230
 231 Figure 9: Statistical distribution of fatigue life “N” and Weibull fitting for both series

232 In both cases the Weibull curves show a good fitting, with R^2 values of 0.960 and 0.944 respectively.

233 On the basis of these data, it is possible to define an S-N- P_f curve, in which the correlation between stress level, number
 234 of cycles, and failure probability is established. In this case, the Aas-Jakobsen’s S-N Expression is proposed [46-49] (eq. 3):

$$S = 1 - \beta \cdot (1 - R) \cdot \log_{10} N \quad (3)$$

235 where S is the relative stress level, R is the ratio between the maximum and the minimum stress values and β is a coefficient
 236 which represents the slope of the S-log(N) straight line [6]. Table 3 shows the values of β for both series.

237

238 Table 3: Representative fatigue life for both series and β coefficient.

	N_{cr}	β
R-Series	2260	0.113

M-Series	71094	0.110
----------	-------	-------

239

240

241

242

243

244

245

246

247

248

249

250

251

Table 5 shows that β is almost identical in both cases. This means that neither the fiber content nor the fiber orientation have influence on the parameter β . In consequence, β will only depend on the concrete matrix. This result agrees with the findings obtained by several research works [14, 26 and 27]. In these works, different concrete mixtures were performed considering different percentage of fibers, ranging from 0% (plain concrete) to 2%. The results of these research works also show almost identical S-N curves in all cases. Fibers alter the internal microstructure. However, this fact has no relevant influence on the fatigue life of the concrete specimen under tensile stress.

The above observation is not synonymous with the fiber content and/or the fiber orientation having no influence on the fatigue life. It is noteworthy that S is the relative stress value, i.e. the quotient between the maximum stress value σ_{max} and the flexural tensile strength of the concrete $f_{ct,fl,pre}$, obtained from the precracking test. The fiber content and orientation influence the value of $f_{ct,fl,pre}$. The higher the fiber content, the higher the value of $f_{ct,fl,pre}$, and the higher the efficiency index, the higher the value of $f_{ct,fl,pre}$. However, when the same relative maximum tensile strength S_{max} is applied to different concrete mixtures, showing different fiber content and/or fiber orientation, the fatigue life is the same.

252

3.2 Static testings of the specimens previously subjected to cyclic load

253

254

255

As explained before, some of the prisms were subjected to cyclic loads up to predefined level of damage. According to the Palmgren-Miner criterion, damage is defined as the quotient between the number of cycles and the fatigue life. In this case, fatigue life has been defined as the number of cycles showing a failure probability of 0.2 (Table 5).

256

257

258

For the R-Series, four groups of 7 prisms each were tested until reaching damage levels of 0.00, 0.20, 0.80 and 0.90, respectively. During the cyclic test, one specimen in the third group and one specimen in the fourth group collapsed before reaching the preset number of cycles.

259

260

261

Moreover, four groups of 4 prisms each were tested for the M-Series, up until damage levels of 0.00, 0.03, 0.28, and 2.81, respectively. In this case, during the cyclic test, one specimen belonging the fourth group collapsed, before reaching the preset number of cycles.

262

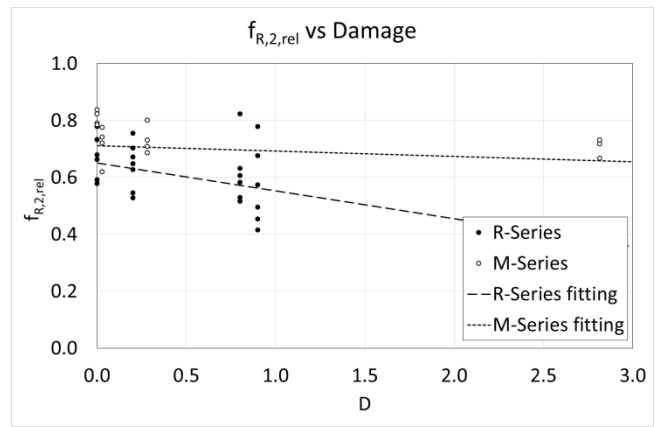
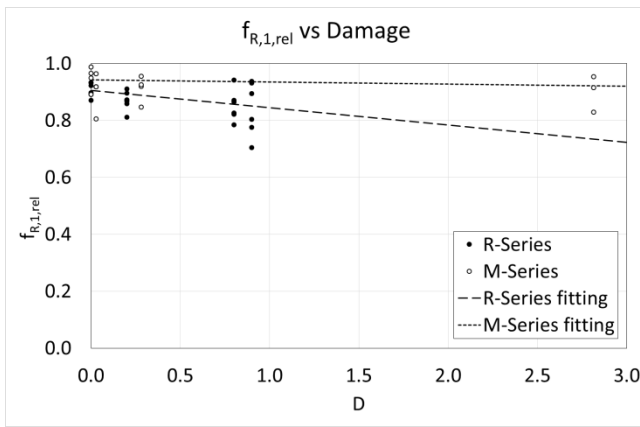
263

264

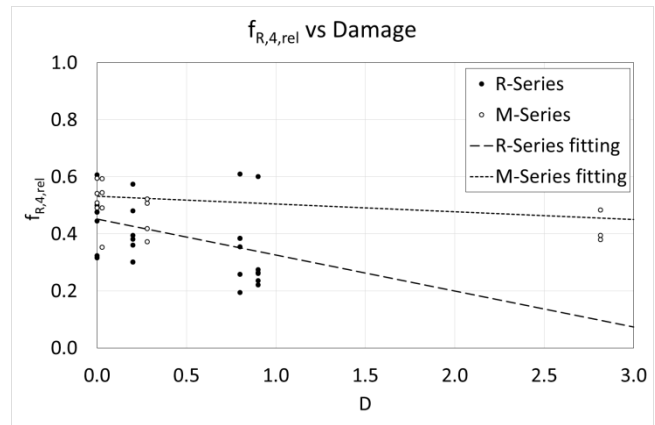
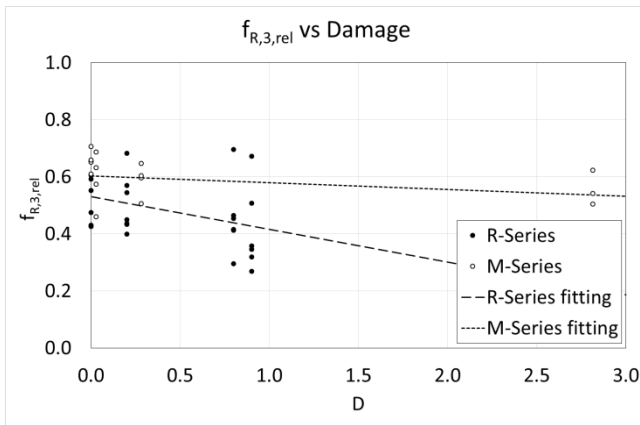
Figure 10 shows the values of the relative residual tensile strength ($f_{R,i,rel}$) for the both series and for the different values of damage [4, 6]. In addition, trend lines are drawn, for easy visualization of the variation in the relative residual tensile strength of the damage.

265

266



267



268

Figure 10: Variation of the relative residual tensile strength to the damage, for both series.

269

270

271

272

273

274

275

276

277

As can be observed in Figure 10, in all the cases, the relative residual tensile strength decreased with the damage. This decrease can be observed in both the R-Series and the M-Series. In the case of the R-Series, the trend lines are always placed below those of the M-Series. Furthermore, these lines show a decreasing slope greater than those of the M-Series. This is directly related to the fiber content. It is clearly observed that the higher the fiber content, the higher the relative residual tensile strength.

Figure 11 shows these same data in a different way, i.e. it shows the correlation between the relative residual tensile strength with the crack width (w), for the different damage and for the different series [4, 6]. Additionally, trend lines have been drawn, in order to easily visualize the variation of the relative residual tensile strength to the crack width.

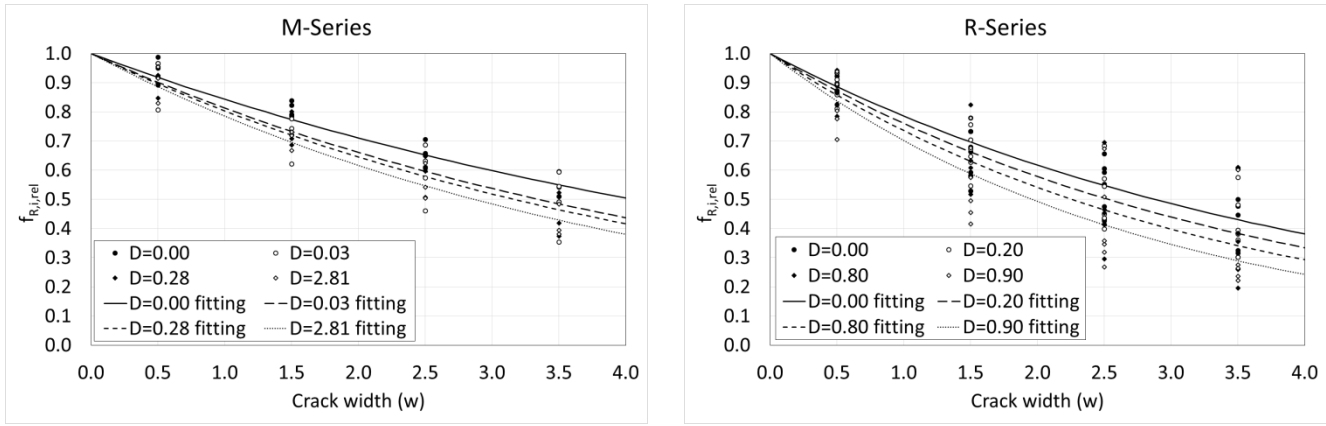


Figure 11: Variation of the relative residual tensile strength to the crack width, for both series.

Again, it can be observed that the trend lines show a progressive decrease with the damage, i.e., the higher the damage, the higher the negative slope of the line is. This behavior is observed in both series.

It can again be seen that the trend lines show a progressive decrease with the damage, i.e., the higher the damage, the higher the negative slope of the line; a behavior observed in both series.

When both series were compared, it was noted that the trend lines of the M-Series showed a smaller slope than those of the R-Series, which demonstrate again that the relative residual tensile strength is inversely proportional to the fiber content.

In the work carried out by Gonzalez and co-workers in 2018 [4], an exponential fitting is proposed for the average values of relative residual tensile strength, which is as follows (eq. 4).

$$f_{R,i,rel} = \exp\{-a_D \cdot w\} \quad i:=1 \text{ to } 4 \quad (4)$$

where, $f_{R,i,rel}$ is the relative residual tensile strength, ($i:=1$ to 4) and w is the crack width. The fitting coefficient, a_D , depends on the damage. Table 4 shows the values of a_D for the different damage values in both series. Additionally, Figure 12 shows these values in a graphic way with their fitted curves.

Table 4: Values of a_i for both series, depending on the damage levels.

R-Series			M-Series		
D	a_i	R^2	D	a_i	R^2
0.00	0.241	0.940	0.00	0.171	0.990
0.20	0.274	0.945	0.03	0.207	0.994
0.80	0.307	0.954	0.28	0.219	0.971
0.90	0.354	0.965	2.81	0.242	0.997

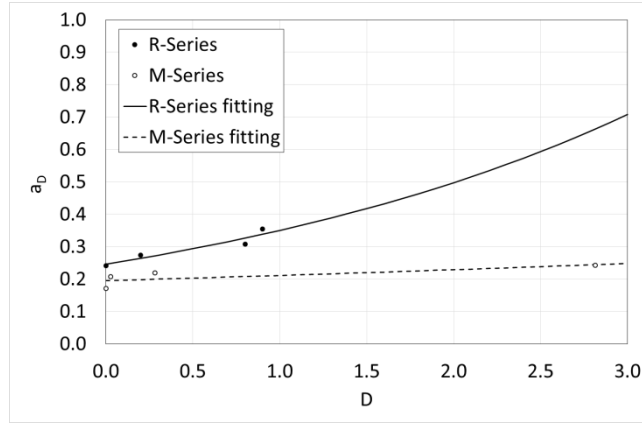


Figure 12: Values of a_D for both series, depending on the damage levels

295

296

297

298

299

300

301

302

303

304

305

306

307

308

309

In Table 6 and Figure 12, the M-Series show smaller values of a_D for all damage levels. Furthermore, the increase of a_D is greater in the case of the R-Series than in the case of M-Series, which once again shows that a_D depends on the fiber content, in such a way that the higher the fiber content, the smaller the slope of the curve a_D vs D . Moreover, the fiber orientation influences the behavior, especially of the crack-bridging fibers.

Two extreme cases may be studied, in order to develop a proper physically compatible equation for a_D .

The first extreme case is, on the one hand, when the fiber content is zero, that is, plain concrete. In this case, $a_i = \infty$ because, plain concrete shows null values of relative residual tensile strength.

On the other hand, when the fiber content increases, a_D decreases, which also implies loss of relative residual tensile strength (see eq. 4). In an extreme case, when the fiber content is 100%, the hypothesis of $a_i = 0$ is considered.

Regarding fiber orientation, when the efficiency index is zero, fibers are placed parallel to the crack surface, $a_i = \infty$, and the behavior is not dissimilar to plain concrete. In addition, when the efficiency index increases, a_D decreases.

According to these criteria, the following fitting formula is proposed (eq. 5):

$$a_i = \frac{\alpha}{e^{i_y}} \cdot \left(\frac{100 - f}{f} \right)^{0.7} \exp \left\{ \beta \cdot \left(\frac{100 - f}{f} \right)^{2.1} \cdot D \right\} \quad (5)$$

310

where, f is the fiber content (in percent), and α and β are two fitting coefficients. This equation is compatible with the above-mentioned criteria. In this case, the best fitting is obtained for $\alpha = 6.90 \cdot 10^{-3}$ and $\beta = 2.27 \cdot 10^{-5}$.

312

313

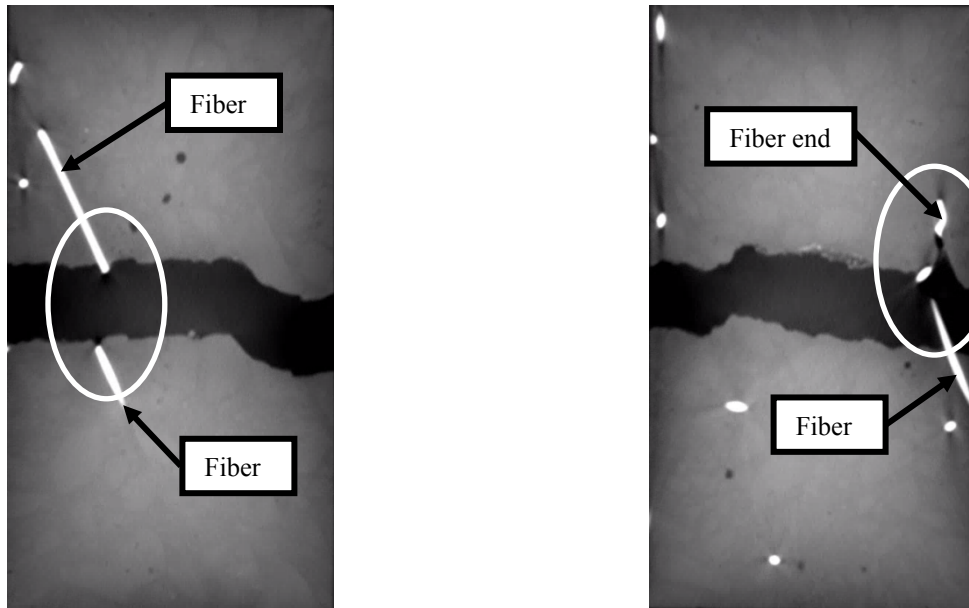
4. FAILURE MECHANISMS

314

Using the CT-Scan, it is possible to visualize the failure mechanisms that occur inside the prism, in areas surrounding the crack. In general, two mechanisms can be observed: fiber breakage and failure of the fiber anchorage. The first one depends

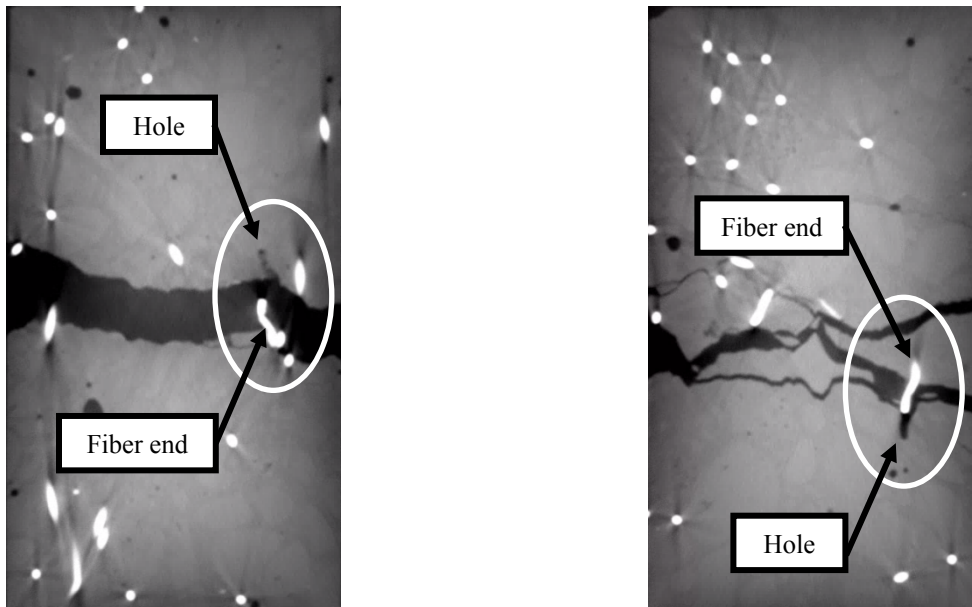
315

316 only on the mechanical properties of the fiber and in the second one, fiber, concrete matrix and the interface fiber-matrix
317 influence the behavior. Figures 13 to 18 show some slices, obtained through the CT-Scan, where these different failure
318 mechanisms can be observed for both series.



319

320 Figure 13: Two examples of cracked fibers from the R-Series (XY Section). On the left, the fiber crack occurs in the
321 middle of the fiber. On the right, the fiber crack occurs close to the end of the fiber.

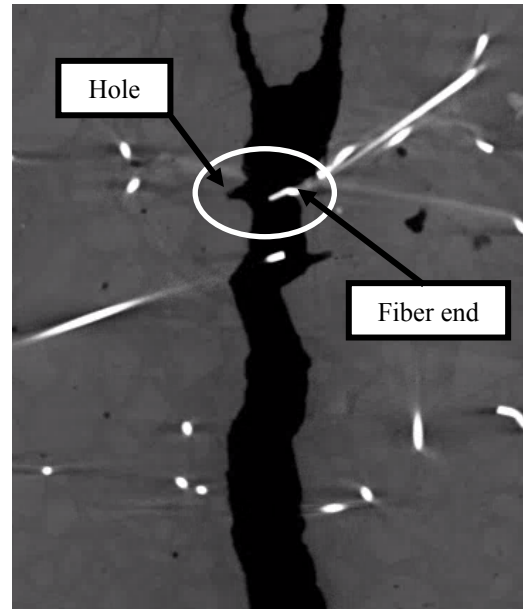
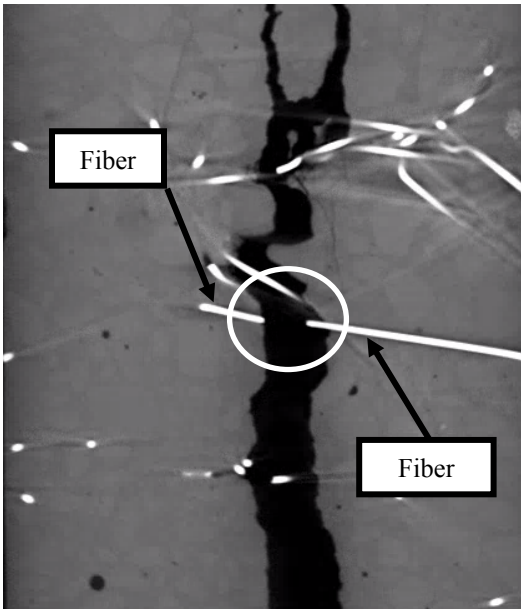


322

323 Figure 14: Two examples of fiber debonding from the R-Series (XY Section). On the left, fiber debonding in the
324 main crack. On the right, fiber debonding in a secondary crack.

325

326

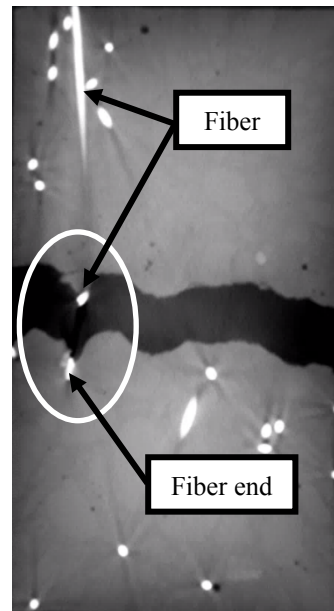
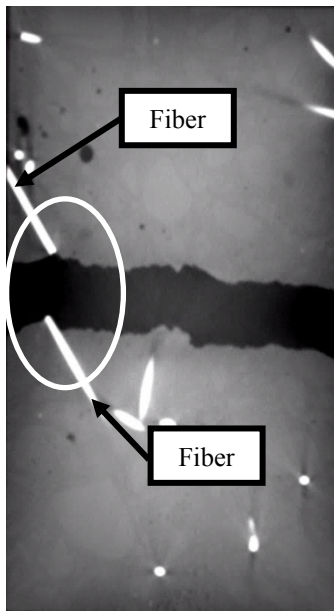


327

328

329

Figure 15: Two examples of crack failure from the R-Series (YZ Section). On the left, a cracked fiber. On the right, fiber debonding.

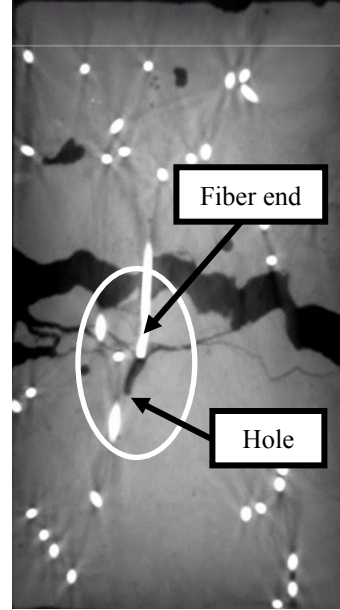
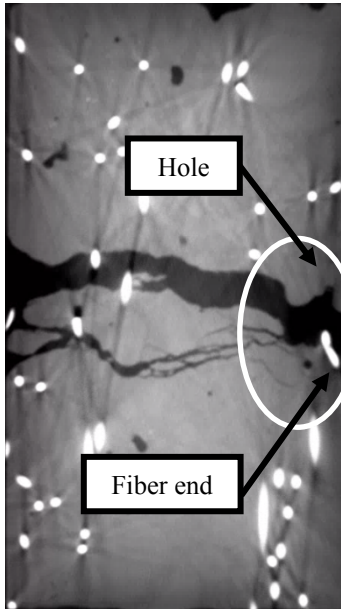


330

331

332

Figure 16: Two examples of cracked fibers from the M-Series (XY Section). On the left, a crack in the middle of the fiber. On the right, a crack close to the end of the fiber.



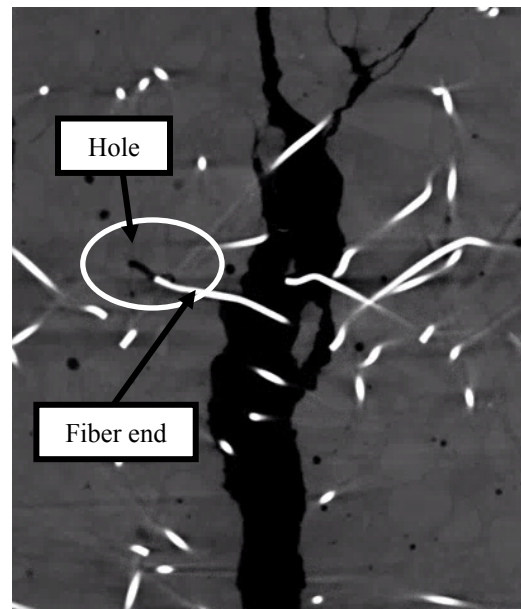
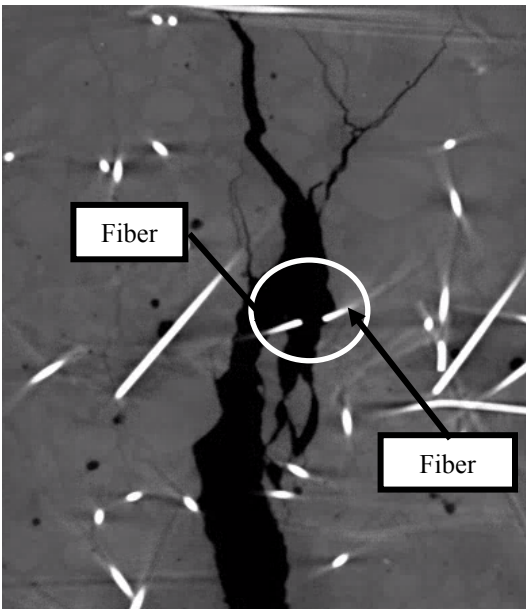
333

334

335

336

Figure 17: Two examples of fiber debonding from the M-Series (XY Section). On the left, fiber debonding in the main crack. On the right, fiber debonding in a secondary crack.



337

338

339

340

Figure 18: Two examples of crack failure from the M-Series (YZ Section). On the left, fiber cracking. On the right, fiber debonding.

341

342

343

The hooked-end fibers used in this work showed good anchoring. Cracks that cross the middle of the fiber tend to break the fiber. When the fiber orientation is perpendicular to the crack surface, the collapse is solely due to tensile forces. However, when the fiber is oblique to the crack surface, which occurs in most cases, the collapse is due to a combination of

344 axial, bending and shear. In this case, the failure directly depends on the tensile strength of the fiber material. Fiber cracking
345 can occur even when the crack crosses the fiber quite close to the fiber anchorage point, (Figures 13b and 14b).

346 On the contrary, when the crack crosses the fiber close to its end, the fiber tends to slip. Because of the shape of the
347 fiber anchorage, a complex stress field forms around the anchorage, which results in tensile stress and concrete cracking. In
348 this case, the failure mechanisms are more complex, as they depend on the fiber, the concrete matrix and the fiber-matrix
349 interface. Fiber debonding results in a hole in the back of the fiber. In this case, it can be observed that the distance between
350 the end of the fiber and the end of the hole provoked by fiber debonding coincides with the crack width.

351 Debonding is more common, i.e., most of the fibers fail because of slippage. The images provided by the CT-Scan
352 show that over 80% of the failures are due to debonding, while less than 20% are due to fiber breakage. This failure mechanism
353 shows a more plastic (post-peak) behavior. The conventional load vs debonding graph shows a linear increase up to a
354 maximum and then a progressive softening. [50-53]. On the contrary, fiber cracking occurs with far less displacement, i.e.,
355 with a much smaller crack opening. In consequence, it seems that the debonding mechanism is the one which provides the
356 post-peak softening behavior to the fiber-reinforced concrete specimens.

357 In addition, fibers were observed at some distance from the cracked concrete crack and, in consequence, undamaged.
358 This fact allows the “intact” fibers to be studied (Figure 19).

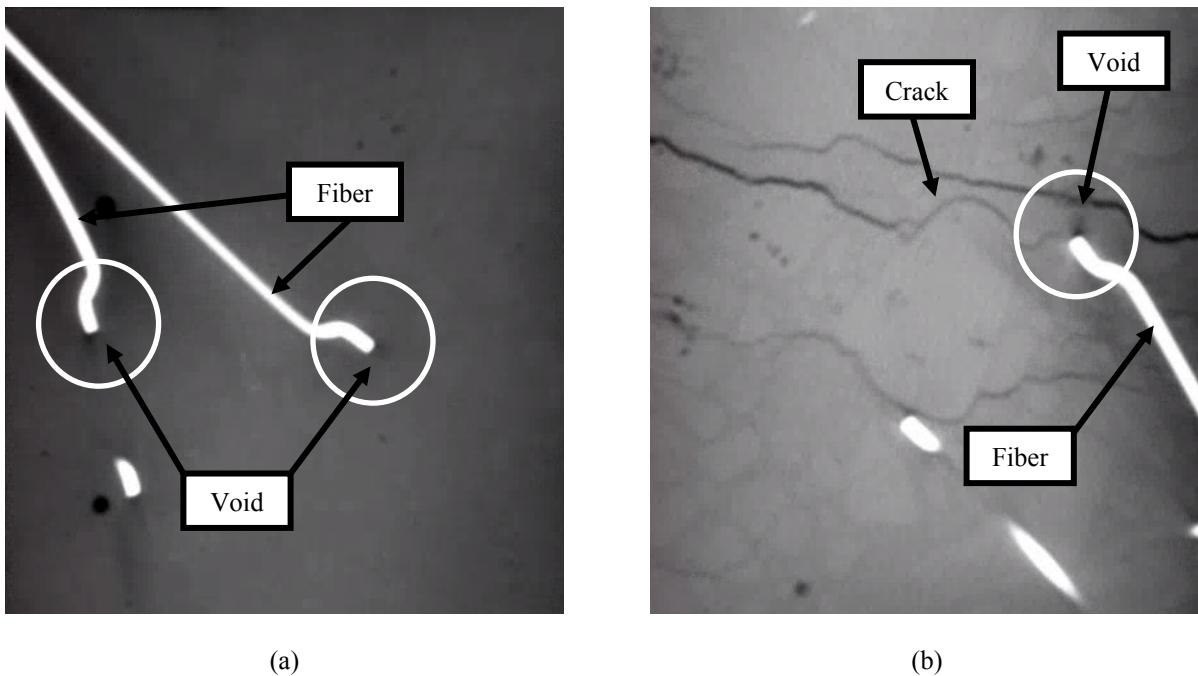


Figure 19: Voids at the end of the fibers (a) and crack initiation (b).

362 Small voids placed at the fiber end (Figure 19a) can be observed, which also facilitated the start of the cracks (Figure
363 19b). This fact indicates that the crack path tends to surround the fiber, resulting in debonding failure instead of breakage
364 failure.

365

366 **5. CONCLUSIONS**

367 In this work, the behavior under cyclic loading of two mixtures of steel-fiber-reinforced concrete has been studied.
368 Both mixtures had the same dosages and only differed in their fiber percentages. The R-Series contained 1% of fibers (by
369 volume), while the M-Series contained 2% of fibers. Prismatic specimens 150x150x600 mm were cast. The specimens were
370 subjected to a 3-point bending testing.

371 Based on the individual fatigue life of the specimens, the characteristic fatigue life has been estimated and compared
372 for both series. The specimens were subjected to a pre-defined damage level and then to a static test, after which their residual
373 tensile strength was measured.

374 In addition, once the specimen was tested and broken, a small sample was extracted from the surrounding of the crack
375 and scanned using a CT-Scan, in order to measure the fiber orientation.

376 The CT-Scan results showed very similar fiber orientations in both cases. The fibers were mainly oriented along the
377 horizontal plane. In the case of the R-Series, the fibers tended to be oriented along the longitudinal axis of the specimen, while
378 in the M-Series, the fibers showed no preferential orientation along the horizontal plane. However, the difference was not
379 very relevant between both series. In addition, the average fiber content that was measured was, in both cases, very close to
380 the expected content.

381 Regarding fatigue behavior, the results have shown that the S-N curves were substantially parallel in both cases. The
382 coefficient β , which represents the slope of the S-N curve, was almost identical in both mixtures. Hence, the fiber density had
383 no influence on the S-N curve. The fiber content modified the concrete tensile strength, but under the same maximum fatigue
384 stress level, the expected fatigue life was the same regardless of fiber content.

385 On the contrary, when the specimens were subjected to a cyclic test up to a pre-defined damage level (defined as the
386 quotient between the number of applied cycles and the fatigue life), and then subjected to a static test up to failure, the results
387 showed that the residual tensile strength strongly depended on fiber content. The M-Series (which showed the highest fiber
388 content) showed higher residual tensile strength values at every crack opening, and a lower loss of residual tensile strength
389 with the damage.

390 The CT-Scan has also provided information on the failure mechanisms. The results show that the debonding failure
391 mechanism was the most frequent, reaching more than 80% of total fiber failure. Only less than 20% of the failures were due

392 to fiber breakage. The failure due to the debonding of the fibers showed a more ductile behavior, while the failure due to
393 breakage of the fibers showed a less ductile behavior. In consequence, it appears that the debonding mechanism provided the
394 post-peak softening behavior in the fiber-reinforced concrete specimens.

395 The scans of the undamaged fibers revealed small voids at the end of the fibers, which also facilitated the initial crack
396 openings. This observation indicates that the crack path tended to surround the fiber, resulting in debonding failure instead of
397 breakage failure.

398

399 **6. ACKNOWLEDGEMENTS**

400 The authors are grateful for financial support from the Ministerio de Economía y Competitividad, BIA2015-68678-
401 C2-R, Spain.

402

403 **REFERENCES**

- 404 [1]. Zia, A.; Ali, M. (2017). "Behavior of fiber reinforced concrete for controlling the rate of cracking in canal-lining.
405 Construction and Building Materials, v 155, pp. 726-739.
- 406 [2]. Mazzoli, A.; Monosi, S.; Plescia, E.S. (2015). "Evaluation of the early-age-shrinkage of Fiber Reinforced Concrete
407 (FRC) using image analysis methods". Construction and Building Materials, v 101, pp: 596-601.
- 408 [3]. Ferrara, L.; Park, Y-D.; Shah, S.P. (2007). "A method for mix-design of fiber-reinforced self-compacting concrete".
409 Cement and Concrete Research, v 37, pp. 957-971.
- 410 [4]. Gonzalez, D.C.; Moradillo, R.; Mínguez, J.; Martínez, J.A.; Vicente, M.A. (2018). "Postcracking residual strengths of
411 fiber-reinforced high-performance concrete after cyclic loading". Structural Concrete, v 19(2), pp. 340-351.
- 412 [5]. Parvez, A.; Foster, S.J. (2015). "Fatigue Behavior of Steel-Fiber-Reinforced Concrete Beams". Journal of Structural
413 Engineering, v 141(4): 04014117: 1 to 8.
- 414 [6]. González, D.C.; Vicente, M.A.; Ahmad, S. (2015). "Effect of cyclic loading on the residual tensile strength of steel
415 fiber-reinforced high-strength concrete". Journal of Materials in Civil Engineering, v 27(9): 04014241: 1 to 8.
- 416 [7]. Zhang, J.; Stang, H.; Li, V.C. (1999). "Fatigue life prediction of fiber reinforced concrete under flexural load".
417 International Journal of Fatigue, v 21, pp. 1033-1049.
- 418 [8]. Mínguez, J.; González, D.C.; Vicente, M.A. (2018). "Fiber geometrical parameters of fiber-reinforced high strength
419 concrete and their influence on the residual post-peak flexural tensile strength". Construction and Building Materials,
420 v 168, pp. 906-922.

- 421 [9]. Bischoff, P.H. (2003). "Tension stiffening and cracking of steel fiber-reinforced concrete". *Journal of Materials in*
422 *Civil Engineering*, v 15(2), pp. 174-182.
- 423 [10]. Al Rikabi, F.T.; Sargand, S.M.; Khoury, I.; Hussein, H.H. (2018). "Material properties of synthetic fiber-reinforced
424 concrete under freeze-thaw conditions". *Journal of Materials in Civil Engineering*, v 30(6): 04018090, 1 to 13.
- 425 [11]. Niu, D.; Jiang, L.; Bai, M.; Miao, Y. (2013). "Study of the performance of steel fiber reinforced concrete to water and
426 salt freezing condition". *Materials and Design*, v 44, pp. 267-273.
- 427 [12]. Medeiros, A.; Zhang, X.; Ruiz, G.; Yu, R.C.; Velasco, M.S.L. (2015). "Effect of the loading frequency on the
428 compressive fatigue behavior of plain and fiber reinforced concrete". *International Journal of Fatigue*, v 70, pp. 342-
429 350.
- 430 [13]. Poveda, E.; Ruiz, G.; Cifuentes, H.; Yu, R.C.; Zhang, X. (2017). "Influence of the fiber content on the compressive
431 low-cycle 585 fatigue behavior of self-compacting SFRC". *International Journal of Fatigue*, v 101, pp. 9-17.
- 432 [14]. Goel, S.; Singh, S.P.; Singh, P. (2012). "Flexural fatigue strength and failure probability of Self Compacting Fibre
433 Reinforced Concrete beams". *Engineering Structures*, v 40, pp. 131-140.
- 434 [15]. Singh, S.P.; Sharma, U.K. (2007). "Flexural fatigue strength of steel fibrous concrete beams". *Advances in Structural*
435 *Engineering*, v 40(2), pp. 197-207.
- 436 [16]. Singh, S.P., Mohammadi, Y.; Kaushik, S.K. (2005). "Flexural fatigue analysis of steel fibrous concrete containing
437 mixed fibers". *ACI Materials Journal*, v 102(6), pp. 438-444.
- 438 [17]. Bajaj, V.; Singh, S.P.; Singh, A.P. et al (2012). "Flexural fatigue analysis of hybrid fibre-reinforced concrete".
439 *Magazine of Concrete Research*, v 64(4), pp. 361-373.
- 440 [18]. Mohammadi, Y.; Kaushik, S.K. (2005) "Flexural fatigue-life distributions of plain and fibrous concrete at various
441 stress levels". *Journal of Materials in Civil Engineering*, v 17(6), pp. 650-658.
- 442 [19]. Singh, S.P.; Kaushik, S.K. (2001). "Flexural fatigue analysis of steel fiber-reinforced concrete". *ACI Materials Journal*,
443 v 98(4), pp 306-312.
- 444 [20]. Plizzari, G.A.; Cangianno, S.; Cere, N. (2000). "Postpeak behavior of fiber-reinforced concrete under cyclic tensile
445 loads". *ACI Materials Journal*, v 97(2), pp. 182-192.
- 446 [21]. Graeff, A.G.; Pilakoutas, K.; Neocleous, K., et al (2012) "Fatigue resistance and cracking mechanism of concrete
447 pavement reinforced with recycled steel fibres recovered from post-consumer tyres". *Engineering Structures*, v 45, pp.
448 385-395.
- 449 [22]. Li, H.; Zhang, M.; Ou, J. (2007). "Flexural fatigue performance of concrete containing nano-particles for pavement".
450 *International Journal of Fatigue*, v 29(7), pp. 1292-1301.

- 451 [23]. Patel, P.A.; Desai, A.K.; Desai, J.A. (2013) "Evaluation of RC and SFRC exterior beam-column joint under cyclic
452 loading for reduction in lateral reinforcement of the joint region". Magazine of Concrete Research, v 65(7), pp. 405-
453 414.
- 454 [24]. Zhang, Y.; Harries, K.A.; Yuan, W. (2013). "Experimental and numerical investigation of the seismic performance of
455 hollow rectangular bridge piers constructed with and without steel fiber reinforced concrete". Engineering Structures,
456 v 58, pp. 255-265.
- 457 [25]. Shah A.; Abid, Ribakov Y. (2011) "Recent trends in steel fiber high-strength concrete". Materials and Design, v 32,
458 pp. 4122-4151.
- 459 [26]. Banjara, N.K.; Ramanjaneyulu, K. (2018). "Experimental Investigations and Numerical Simulations on the Flexural
460 Fatigue Behavior of Plain and Fiber-Reinforced Concrete". Journal of Materials in Civil Engineering, v. 30(8):
461 04018151, 1 to 15.
- 462 [27]. Johnston, C.D.; Zemp, R.W. (1991). "Flexural Fatigue Performance of Steel Fiber Reinforced Concrete – Influence of
463 Fiber Content, Aspect Ratio and Type". ACI Materials Journal, n° 88-M44, pp. 374-383.
- 464 [28]. Bernardo, H.; Vicente, M.A.; González, D.C.; Martínez, J.F. (2015). "Efecto de las cargas cíclicas sobre la adherencia
465 hormigón-acero en hormigones sumergidos". Hormigón y Acero, v 66(276), pp. 225-236.
- 466 [29]. Vicente, M.A.; González, D.C.; Mínguez, J.; Martínez, J.A. (2014). "Residual modulus of elasticity and maximum
467 compressive strain in HSC and FRHSC after high-stress-level cyclic loading". Structural Concrete, v. 15(2), pp. 210-
468 218.
- 469 [30]. Bernardo, H.; Vicente, M.A.; González, D.C.; Martínez, J.F. (2014). "Cyclic bond testing of steel bars in high-
470 performance underwater concrete". Structural Engineering International, v 24(1), pp. 37-44.
- 471 [31]. Vicente, M.A.; González, D.C.; Martínez, J.A. (2014). "Mechanical Response of Partially Prestressed Precast Concrete
472 I-Beams after High-Range Cyclic Loading." Pract. Period. Struct. Des. Constr., 10.1061/(ASCE)SC.1943-
473 5576.0000225, 04014022.
- 474 [32]. Urban, S.; Strauss, A.; Macho, W.; Bergmeister, K.; Dehlinger, C. and Reiterer, M. "Zyklisch belastete
475 Betonstrukturen. Robustheits- und Redundanzbetrachtungen zur Optimierung der Restnutzungsdauer (Concrete
476 structures under cyclic loading. Robustness and redundancy considerations for residual lifetime optimization) (In
477 German)". Bautechnik, vol. 89, no 11, 2012,
- 478 [33]. Zanuy, C.; Albajar, L.; De la Fuente P. (2011). "The fatigue process of concrete and its structural influence," Materiales
479 de Construcción, v 61(303), pp. 385-399.

- 480 [34]. Zanuy, C.; Albajar, L.; de la Fuente, P. (2009). "Sectional analysis of concrete structures under fatigue loading", *ACI*
481 *Struct. J.*, v 106(5), pp. 667-677.
- 482 [35]. Zhang, B.; Wu, K. (1997). "Residual fatigue strength and stiffness of ordinary concrete under bending" *Cement and*
483 *Concrete Research*, v 27(1), pp. 115-126.
- 484 [36]. International Federation for Structural Concrete. (2010). "Model code for concrete structures." *FIB Bulletin* 65,
485 Lausanne, Switzerland.
- 486 [37]. Vicente, M.A.; Ruiz, G.; González, D.C.; Mínguez, J.; Tarifa, M.; Zhang, X. (2018). "CT-Scan study of crack patterns
487 of fiber-reinforced concrete loaded monotonically and under low-cycle fatigue". *International Journal of Fatigue*, v.
488 114, pp. 138-147.
- 489 [38]. Balazs, G.L.; Czoboly, O.; Lubloy, E.; Kapitany, K.; Barsi, A. (2017). "Observation of steel fibers in concrete with
490 computed tomography". *Construction and Building Materials*, v. 140, pp. 534-541.
- 491 [39]. Pastorelli, E.; Herrmann, H. (2016). "Time-efficient automated analysis for fibre orientations in steel fibre reinforced
492 concrete". *Proceedings of the Estonian Academy of Sciences*, v 65 (1), pp. 28-36.
- 493 [40]. Herrmann, H.; Pastorelli, E.; Kallonen, A.; Suuronen, J.P. (2016). "Methods for fibre orientation analysis of X-ray
494 tomography images of steel fibre reinforced concrete (SFRC)". *Journal of Materials Science*, v 51(8), pp. 3772-3783.
- 495 [41]. Ponikiewski, T.; Katzer, J. (2016). "X-ray computed tomography of fibre reinforced self-compacting concrete as a tool
496 of assessing its flexural behaviour". *Materials and Structures*, v. 49, pp. 2131-2140.
- 497 [42]. Ponikiewski, T.; Katzer, J.; Bugdol, M.; Rudzki, M. (2014). "Determination of 3D porosity in steel fibre reinforced
498 SCC beams using X-ray computed tomography". *Construction and Building Materials*, v 68, pp. 333-340.
- 499 [43]. Vicente, M.A.; González, D.C.; Mínguez, J. (2014). "Determination of dominant fibre orientations in fibre-reinforced
500 high strength concrete elements based on computed tomography scans". *Nondestructive Testing and Evaluation*, v
501 29(2), pp. 164-182.
- 502 [44]. Vicente, M.A.; Mínguez, J.; González, D.C. (2017). "The use of computed tomography to explore the microstructure
503 of materials in civil engineering: from rocks to concrete". In: Halefoglu Ahmet Mesrur, editor. *Computed tomography*
504 *- advanced applications*. InTech.
- 505 [45]. European Committee for Standardization (2004). "EUROCODE 2, Design of concrete structures". *Eurocode2*,
506 Brussels, Belgium.
- 507 [46]. Aas-Jakobsen, K. (1970). "Fatigue of concrete beams and columns." *Institutt for betonkonstruksjoner*, NTH
508 Trondheim, Trondheim, Norway, 148.
- 509 [47]. Hsu, T.T.C. (1981). "Fatigue of plain concrete." *ACI Journal of Materials*, v. 78, pp. 292-305.

- 510 [48]. Tepfers, R. (1979). "Tensile fatigue strength of plain concrete." *ACI Journal*, v. 76, pp. 919–933.
- 511 [49]. Oh, B.H. (1986). "Fatigue analysis of plain concrete in flexure". *Journal of Structural Engineering*, v. 112:2, pp. 306–
512 312.
- 513 [50]. Bhutta, A.; Farooq, M.; Borges, P.H.R.; Banthia, N. (2018). "Influence of fiber inclination angle on bond-slip behavior
514 of different alkali activated composites under dynamic and quasi-static loadings". *Cement and Concrete Research*, v.
515 107, pp. 236-246.
- 516 [51]. Wu, Z.; Khayat, K.H.; Shi, C. (2018). "How do fiber shape and matrix composition affect fiber pullout behavior and
517 flexural properties of UHPC?" *Cement and Concrete Composites*, v. 90, pp. 193-201.
- 518 [52]. Lee, S.F.; Jacobsen, S. (2011). "Study of interfacial microstructure, fracture energy, compressive energy and
519 debonding load of steel fiber-reinforced mortar". *Materials and Structures*, v. 44 (8), pp. 1451–1465.
- 520 [53]. Wille, K.; Naaman, A.E. (2012). "Pullout behavior of high-strength steel fiber embedded in ultra-high-performance
521 concrete" *ACI Journal of Materials*, v. 109 (4), pp. 479–487.

AUTHORS STATEMENT FOR PUBLICATION


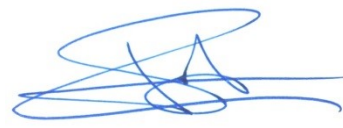

Manuscript title: COMPUTED TOMOGRAPHY SCANNING OF THE INTERNAL MICROSTRUCTURE, CRACK MECHANISMS, AND STRUCTURAL BEHAVIOR OF FIBER-REINFORCED CONCRETE UNDER STATIC AND CYCLIC BENDING TESTS

Corresponding author's full name: MIGUEL A. VICENTE

Please note that all contributing authors are obligated to sign *Authors statement for publication* form otherwise the manuscript will not be published.

Please fill in the table below according to following:

- *list the authors in order in which they are stated in manuscript. This way each author is assigned with number for further identification.*
- *each author should sign this document (on designated place in the table). By signing this form authors take full responsibility for all statements it contains.*

No.	Author's full name (in capital letters)	Author's signature
1.	MIGUEL A. VICENTE	
2.	JESÚS MÍNGUEZ	
3.	DORYS C. GONZÁLEZ	

AUTHORSHIP STATEMENT:

Please fill the table with numerical code of each author (from the before signed table) regarding authors contribution to specific component of research.

Component of the research	Author's number
substantial contribution to conception and design	1, 2 and 3
substantial contribution to acquisition of data	2 and 3
substantial contribution to analysis and interpretation of data	1 and 2
drafting the article	1 and 3
critically revising the article for important intellectual content	1, 2 and 3
final approval of the version to be published	1, 2 and 3

Please tick the box if the statement applies:

- ✓ to the best of your knowledge everybody who participated substantially in the study is not omitted from the article
- ✓ to the best of your knowledge, all persons listed as authors qualify for authorship

All persons who have made substantial contributions to the work but do not meet the criteria for authorship are listed in Acknowledgments section (technical help, writing assistance, general support, financial and material support)

Yes No

All persons named in the Acknowledgment section of the manuscript have given their permission to be named

Yes No

ORIGINALITY OF THE WORK STATEMENT:

Please tick the box if the following statements are correct to the best of your knowledge:

- ✓ the manuscript is not previously published in the same or very similar form in other journal (previous publishing does not apply to abstract or poster presentations at a professional meeting)
- ✓ the manuscript is not currently under consideration in other journals (that does not apply for manuscripts that have been rejected by other journals)

RESEARCH ETHICS:

The Editorial board may require proof of ethics committee approval. Do **not** send original documents to the Journal but be sure to archive it for further purposes.

Reported research was approved by institutional/national ethics committee:

- Yes
- No
- Not applicable

If yes, please state the name and location of the approving ethics committee:

If no, please provide further details:

PATIENT PRIVACY AND CONFIDENTIALITY:

The Editorial board may require proof of participant consent. Do **not** send original documents to the Journal but be sure to archive it for further purposes.

The appropriate informed consent was obtained from all research participants:

- Yes
- No
- Not applicable

If no, please explain:

Date (25/11/2018)

Corresponding author's signature

A handwritten signature in blue ink, consisting of a stylized, cursive script that is difficult to decipher. The signature is written over a horizontal line.